Dual-Purpose Canister Filling Demonstration Project Progress Report

Spent Fuel and Waste Disposition

Prepared for
US Department of Energy
Spent Fuel and Waste Science and Technology

Nesrin O. Cetiner, Emilian Popov, Eliott J. Fountain, Venugopal K. Varma, Kaushik Banerjee
Oak Ridge National Laboratory

February 15, 2019
M3SF-19OR0103050115
ORNL/SPR-2019/1086

This is a technical report that does not take into account the contractual limitations under the Standard Contract for Disposal of Spent Nuclear Fuel and/or High-Level Radioactive Waste (Standard Contract) (10 Code of Federal Regulations [CFR] Part 961). Under the provisions of the Standard Contract, the Department of Energy (DOE) does not consider spent nuclear fuel (SNF) in multi-assembly canisters to be an acceptable waste form, absent a mutually agreed to contract amendment. To the extent discussions or recommendations in this presentation conflict with the provisions of the Standard Contract, the Standard Contract provisions prevail.

ABSTRACT

This report discusses the initial progress made at the Oak Ridge National Laboratory to support direct disposal of dual-purpose canisters (DPCs) using filler materials to demonstrate that the probability of criticality in DPCs during disposal to be below the probability for inclusion in a repository performance assessment. In the initial phase of a multi-phase effort that will result in a full-scale demonstration, a computational fluid dynamics (CFD) model was developed to gauge the filling process and to uncover any unforeseen issues. The initial filling simulations of the lower region (mouse holes) of a prototypic DPC show successful removal of the inner space voids and smooth, even progression of the liquid level. In the initial phase, flow through a pipe that is similar to the drain pipe in a DPC will be investigated separately to gain valuable insight of flow regime inside a pipe. The initial experimental setups for validating the computational filling model have been designed, and the various assembly parts are being procured. The experience gained from the initial experiments will be applied to the next steps toward a full-scale demonstration and to the validation of multiphysics filling simulation models.

This page is intentionally left blank.

CONTENTS

LIST OF FIGURES

This page is intentionally left blank.

LIST OF TABLES

This page is intentionally left blank.

REVISION HISTORY

Revision	Changes Made
0	Initial issue
1	This revision incudes a description of a flow experiment through a pipe that is similar to the drain pipe in a DPC. This experiment will be used to gain insight into the flow regime inside a narrow, long pipe. All updates are identified by black vertical lines in the margin.
2	Minor editorial changes throughout the document. All updates are identified by black vertical lines in the margin. This revision includes Appendix A, which reports on progress in the CFD filling simulations and initial physical testing efforts supporting simulation validation.

This page is intentionally left blank.

ACRONYMS

BWR	boiling water reactor
CCI	confocal chromatic imaging
CFD	computational fluid dynamics
DOE	US Department of Energy
DOE-NE	US Department of Energy Office of Nuclear Energy
DPC	dual-purpose canister
FCRD	Fuel Cycle Research and Development
FY	fiscal year
IFM	intermediate flow mixer
LDV	laser doppler velocimetry
NRC	Nuclear Regulatory Commission
ORNL	Oak Ridge National Laboratory
PDT	photochromic dye tracing
PIV	particle image velocimetry
PWR	pressurized water reactor
RTV	room temperature vulcanizing
SFP	spent fuel pool
SNF	spent nuclear fuel
UNF-ST&DARDS	Used Nuclear Fuel – Storage, Transportation & Disposal Analysis Resource and Data Systems
VOF	volume of fluid

This page is intentionally left blank.

DUAL-PURPOSE CANISTER FILLING DEMONSTRATION PROJECT PROGRESS REPORT

1. INTRODUCTION

This report documents work performed supporting the US Department of Energy (DOE) Nuclear Energy Spent Fuel and Waste Disposition, Spent Fuel and Waste Science and Technology, under work breakdown structure element 1.08.01.03.05, "Direct Disposal of Dual Purpose Canisters." In particular, this report fulfills the M4 milestone, M4SF-18OR010305015, "Summary status report of DPC filler demonstration project," as Revision 1 to M4SF-18OR010305017, "Unit test plan for filler demonstration," within work package SF-18OR01030501, "Direct Disposal of Dual Purpose Canisters–ORNL."

The commercial US nuclear utilities are currently storing spent nuclear fuel (SNF) onsite in spent fuel pools (SFPs) and dry storage systems. SFPs were initially constructed for temporary storage, but without SNF reprocessing options in the United States and with no final disposal pathway, SFPs started to reach capacity limits. Hence, to allow continued operation of the nation's commercial nuclear fleet, utilities started transferring SNF from SFPs (wet storage) to dry storage. As of June 4, 2018, there were 2,802 dry storage systems in use in the United States containing 117,737 spent fuel assemblies [1]. The majority of the dry storage systems currently being loaded are dual-purpose (storage and transportation) canister (DPCs). DPCs can accommodate up to 37 pressurized water reactor (PWR) assemblies and 89 boiling water reactor (BWR) assemblies, and they are designed primarily for storage and transportation. The DOE Office of Nuclear Energy (NE) is currently investigating the feasibility of direct disposal of DPCs in a geological repository to potentially offset the need to repackage currently loaded SNF into smaller disposal canisters. DPC direct disposal has many potential benefits, including cost savings in terms of billions of dollars, minimization of worker dose incurred from repackaging activities, and reduction of low-level radioactive waste in the form of discarded DPCs [2]. Although it has been indicated [2] that direct disposal of DPCs is feasible from a purely technical perspective, several engineering challenges, along with legal and policy issues, must be addressed to make DPC disposal a reality. One challenge is the potential for post-closure criticality in a repository time frame.

The potential for various DPC designs to achieve post-closure criticality configurations is under investigation using as-loaded DPC-specific criticality analysis. As-loaded criticality analyses of the currently loaded DPCs are being performed using the Used Nuclear Fuel-Storage, Transportation & Disposal Analysis Resource and Data System (UNF-ST&DARDS) [3] to evaluate uncredited margins that can be used to offset an increase in canister reactivity (calculated in terms of neutron multiplication factor, k_{eff}) due to various postulated degradation mechanisms in a repository time frame. Based on current modeling approaches [3], it has been shown that many of the loaded canisters have the potential to achieve criticality under the right conditions over a repository time frame (i.e., 10,000 years or longer) (Figure 1).

As shown in Figure 2, three approaches are under investigation to support post-closure criticality of DPCs in a repository time frame. The first approach is to perform detailed modeling and analysis of each loaded DPC; this effort is underway using UNF-ST&DARDS (Figure 1). The second approach includes a criticality consequence analysis to determine the impact of a potential criticality event on a repository performance assessment. The third approach is to investigate preconditioning of DPCs with engineering filler materials that can be credited over a repository time frame to displace the moderator material. (The introduction of a moderator material is needed to achieve in-canister criticality.) This report presents the progress made at Oak Ridge National laboratory (ORNL) to support adding a filler material to existing DPCs before placing them into a repository.

The work presented in this report focuses on initial evaluation of the filling option using simulations and prototypic (mockup) testing. The objective is to develop a DPC filling simulation that will be used to design a simple experiment of injecting surrogate filling materials through the drain pipe. The experimental data from the simple test will also be used to validate the simulation model. The objective of this simulation and simple test is to determine (1) whether a DPC can be filled using the drain pipe, (2) feasible filling rates, and (3) the volume fraction to be filled. Currently, two classes of engineering filling materials are under consideration: cementitious materials and low-temperature melting metals/alloys. The single physics flow simulation will be developed in phases, resulting in a fully validated multiphysics simulation to support and assess the DPC filling process. The multiphysics simulation will also be used to screen filler materials.

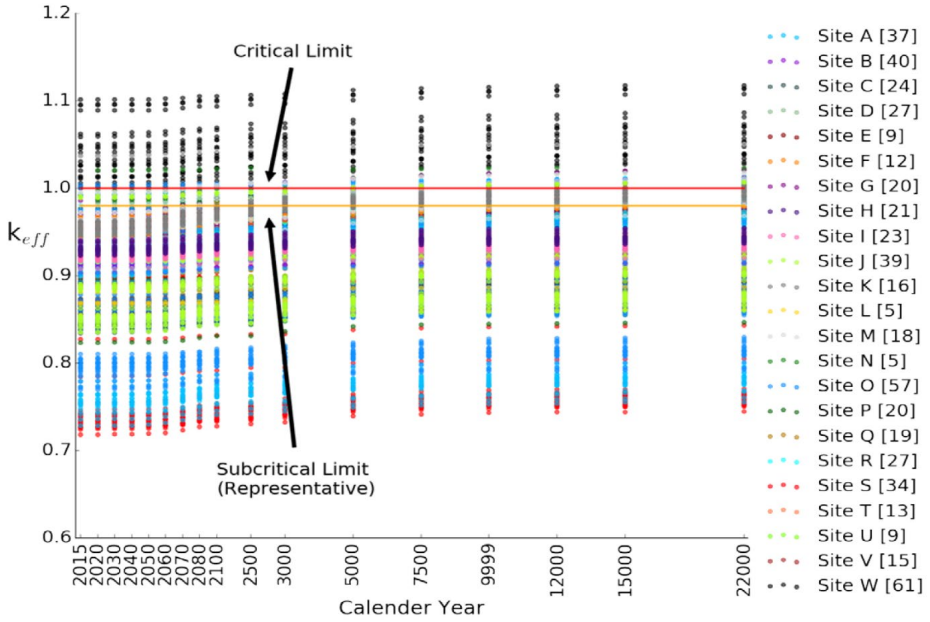

Figure 1. k_{eff} as a Function of the Calendar Year (up to Year 22,000) for 551 DPCs Loaded at 23 Sites. (Postulated degradation scenario includes loss of neutron absorber panels from basket over repository time frame.).

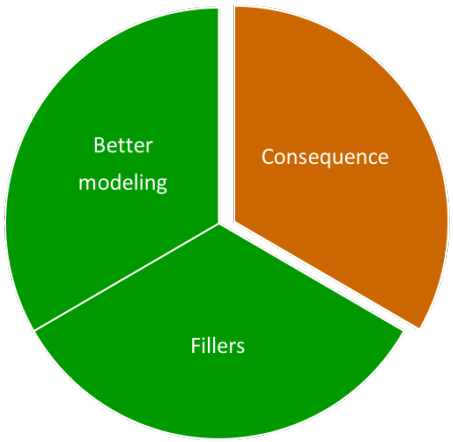

Figure 2. Three Approaches Taken within the Long-Term DPC Disposition Evaluation Program.

This report is presented in two parts. The first part presents the progress made to develop a single physics filling simulation. The second part presents the progress made to develop an experimental setup to (1) validate the numerical simulation and (2) to understand various foreseen and unforeseen issues of filling a DPC from the bottom. The objective is to understand various elements of the filling process and to gradually develop a fully validated simulation and test setup to present all the coupled processes involved in filling a canister with filler materials. This approach will identify a filling method (e.g., filling through the drain pipe, vent, or purpose-built access to the DPC's interior) that can be used with high confidence and to vet various potential filling materials as presented in "Joint Workplan on Filler Investigations for DPCs" [4].

This page is intentionally left blank.

2. FILLING SIMULATION

The objectives of the filling simulations are (1) to numerically analyze the filling process, initially on ideal surfaces, (2) to determine remaining voids and filling times, and (3) to identify potential problems. Simulations provide the flexibility needed to experiment with different liquids (metals) and surrogates, to explore filling methods based on existing or new canister features, to aid the experiment design by scaling major quantities.

A canister mockup test section is designed (Figure 3, see Section 2.4) and simulated. It represents the lower 16% of a real canister (height 74 cm, Ø26 cm), and it includes the passages among the assemblies' shrouds (mouse holes), the support stands (assembly spacer), the assembly's lower grids, and the first spacer grid. The design uses a 5 × 5 rod array, which is considered representative of a PWR fuel bundle. A circular container encloses five 5 × 5 bundles and accounts for most real canister features [5].

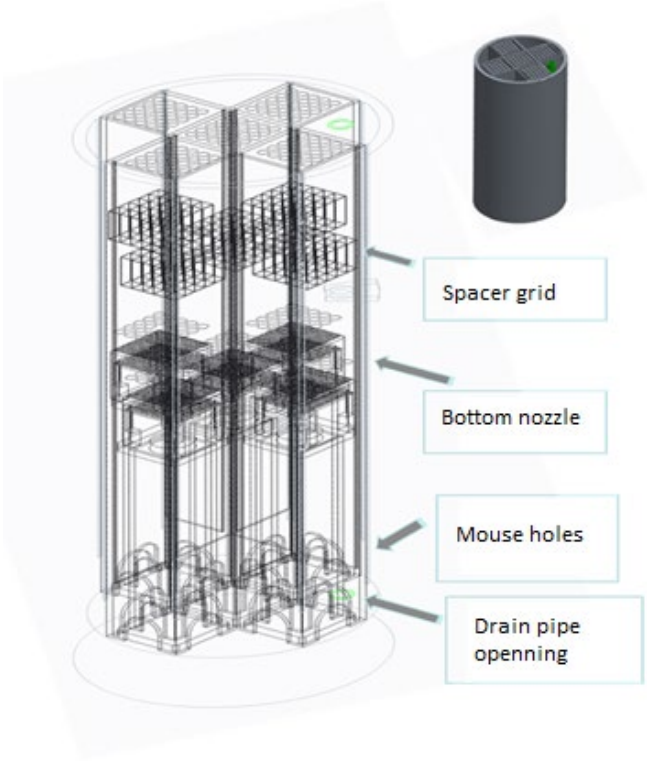

Figure 3. DPC Mockup (Based on 5 × 5 Bundles) of the Lower Section of the Real Canister, Including Mouse Holes, Supports, Bottom Nozzle, and One Spacer Grid.

The simulation employs a 3-dimensional (3D) computational fluid dynamics (CFD) method for a two-phase two-component system in isothermal condition. The gas (helium) and the liquid (metals) front propagation is resolved by solving a viscous flow of mixture [6]. To implement this approach, the commercial software STAR-CCM+ version 13.02 is selected [7]. This model is not suitable for casting (solidification).

The problem is formulated within the framework of the segregated flow approach and discretized by the finite volume method. This includes and allows for coupling between the continuity and momentum

equations. The following integral equations represent the conservation of mass and momentum (Navier-Stokes):

$$\text{Continuity: } \frac{\partial}{\partial t}\int_V \rho dV + \oint_A \rho \bar{V} \cdot da = 0\,, \tag{1}$$

$$\text{Momentum: } \frac{\partial}{\partial t}\int_V \rho \bar{V} dV + \oint_A \rho \bar{V} \otimes \bar{V} \cdot da = -\oint_A pI \cdot da + \oint_A T + \int_V f_g dV\,, \tag{2}$$

where V is volume, A is area, a is area vector, p is pressure, f_g is gravity force, ρ is density, $\bar{V}$ is velocity vector, T is stress tensor, and μ is dynamic viscosity. For laminar flows, the stress tensor is formulated as follows: $T = \mu[\nabla\bar{V} + \nabla\bar{V}^T - \frac{2}{3}(\nabla \cdot \bar{V})I]$, where I is the identity tensor.

To apply the flow model shown above to a filling problem that involves liquid and vapor phases, it is necessary to formulate it as a mixture. Mixture models are formulated using a Eulerian multiphase platform. Additional (phasic) quantities are introduced, all based on the volume fraction of one of the phases, *i*:

$$\rho = \sum_i \rho_i\, \alpha_i; \quad \mu = \sum_i \mu_i\, \alpha_i; \quad c_p = \sum_i \frac{(c_p)_i \rho_i}{\rho}\alpha_i; \;\; where: \; \alpha_i = \frac{V_i}{V} \;\; and \sum_i \alpha_i = 1. \tag{3}$$

Then a transport equation for the volume fraction is added to the system. The model is called *volume of fluid* (VOF) and has been proven to demonstrate accurate results with low computing cost.

$$\frac{\partial}{\partial t}\int_V \alpha_i dV + \oint_A \alpha_i \bar{V} \cdot da = \int_V \left(S_{\alpha_i} - \frac{\alpha_i}{\rho_i}\frac{D\rho_i}{Dt}\right) dV\,, \tag{4}$$

where S_{α_i} is the source void fraction, and $\frac{\alpha_i}{\rho_i}\frac{D\rho_i}{Dt}$ is the material derivative of phase density.

Two types of materials are considered as filler candidates. ORNL is investigating low melting temperature metals and surrogate liquids, and Sandia National Laboratory is studying the use of slurries (concrete mixtures). An initial list of fillers used in numerical simulations is given in Table 1. Note that these are not necessarily candidates for final application but are mainly for numerical simulation in the simple unit test for validation. Two transport properties are important for this phase of the filling evaluation: density and dynamic viscosity. Silicone oils are highly ranked candidates due to their low cost and the large available selection of viscosities.

One half (central symmetry) of the geometry in Figure 3 is initially considered. It has a volume of 11.46 liters per Figure 4). With a volumetric scaling factor to the real geometry of about 6.5, and with an estimate of 17 hours for filling time of the real canister, the equivalent filling rate to be applied within the

model is determined to be 1.26 cm^3/s. Note that this is true for one half of the geometry. For testing, the filling rate of the entire volume must be two times higher. The Reynolds numbers (Re) for such filling rates and length scales, which are typical for rod bundles, are in single digits at Re~3, which justifies the laminar flow regime assumption. The initial mesh of the entire geometry resulted in a computational grid consisting of about 6M elements. The liquid is fed through the inlet section of the drain pipe, as shown in Figure 4. A velocity boundary condition is defined at the drain pipe orifice (area 180 mm^2) with a velocity magnitude of 1.26/180 = 0.007 m/s. Thus, the filling simulation is separated from the drain pipe simulation. The flow regime in the vertical drain pipe is subject to separate evaluation, which is currently under investigation. The formulation of that study is provided below.

Table 1. Preliminary list of liquids for testing and filling simulations.

Material	Melting Temp. (°C)	Density (g/cm^3)	Viscosity (Pa·s)	Reference
Glycerin ($C_3H_8O_3$)	Liquid	1.26@RT	0.95@RT	www.MatWeb.com
Silicon oil (Catalog ID: 378372)	Liquid	0.96@25C	0.33@25C	www.sigmaaldrich.com
Lead	327 (600K)	10.70 @600K	0.0026@600K	V. Sobolev (2007)
Lead-bismuth	124 (398K)	10.53 @398K	0.0032@398K	B. Alchagirov (2003)
Mercury	Liquid	13.53@RT	0.0015@RT	Thermal Fluids Central
Water	Liquid	0.997@RT	0.00088@RT	Web (for comparison)

Calculations are run in parallel on 32–640 computing processors. To properly capture the liquid level progression, the time step must be kept between 1–5 ms. The shortest runtime during this preliminary phase was 0.7 hour for one second of the filling process. Filling the entire geometry would take days of computing, so the strategy was changed. The major objective of a filling simulation is to predict the level progression and the void removal. Both of these occur near the current level position. The areas of computational domain below and above the level have little-to-no influence on the filling, but they consume computing resources. To reduce the computing burden, the domain is decomposed into smaller regions, and a data mapping algorithm is applied. The regions overlap, and the velocity and the void fraction (liquid) are mapped from one region to another. The canister geometry further facilitates this approach because the area above the mouse holes is composed of parallel channels (bundle region), and only one channel needs to be modeled. This radically reduces the computing load.

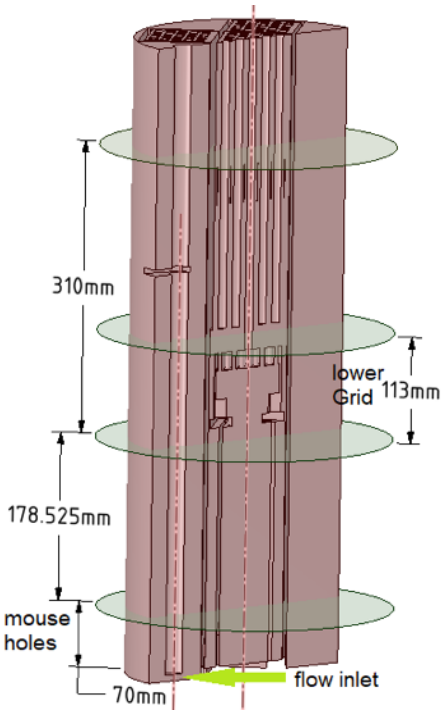

Figure 4. Model Split Indicating the Sections of the Geometry Modeled.

2.1 Filling of the Mouse Hole Region

First the mouse hole region is separated and modeled, as shown in Figure 4. The overall height of the section shown is 70 mm, and it comprises the entire geometry. A polyhedral grid of about 45,000 elements was used. The wall mesh is displayed in Figure 6. It gives a perspective of the geometry with a clear view of the mouse holes. The objective of this simulation is to demonstrate that the mouse holes can be successfully filled if the drain pipe opening provides a continuous constant flow of 1.26 cc/s. The runs are performed on 32 processors for ~5 days (average runtime is 0.12 hour/sec of transient) with a time step of 5 ms. Simulations of the following liquids have demonstrated successful filling of voids in the mouse holes region: glycerin, lead-bismuth, silicone oil, and mercury. Mercury (Hg) is not an option for a real application, but due to its low viscosity and high density, it represents a bounding scenario for the simulation. No noticeable level deformations are observed when different liquids are used. The filling rate is low enough to avoid any local effects that could compromise the filling. This is illustrated in Figure 5. , which plots sections of the mouse hole region for two liquids: lead-bismuth (Pb-Bi) and silicone oil. Even though the densities of these liquids differ by about ten times and the viscosities differ by about hundred times, the filling looks the same. The plot in Figure 5. shows the liquid level at 400 s and at the end of the filling process (total time 1020 s), when the level is at the middle and at the top of the mouse holes. No visible differences are noticeable. The volumes of injected liquids are the same: 496.5 cc for silicone oil, and 498.2 cc for Pb-Bi at 400 s. The small differences are due to computational inaccuracies because the filling rate is the same for both liquids.

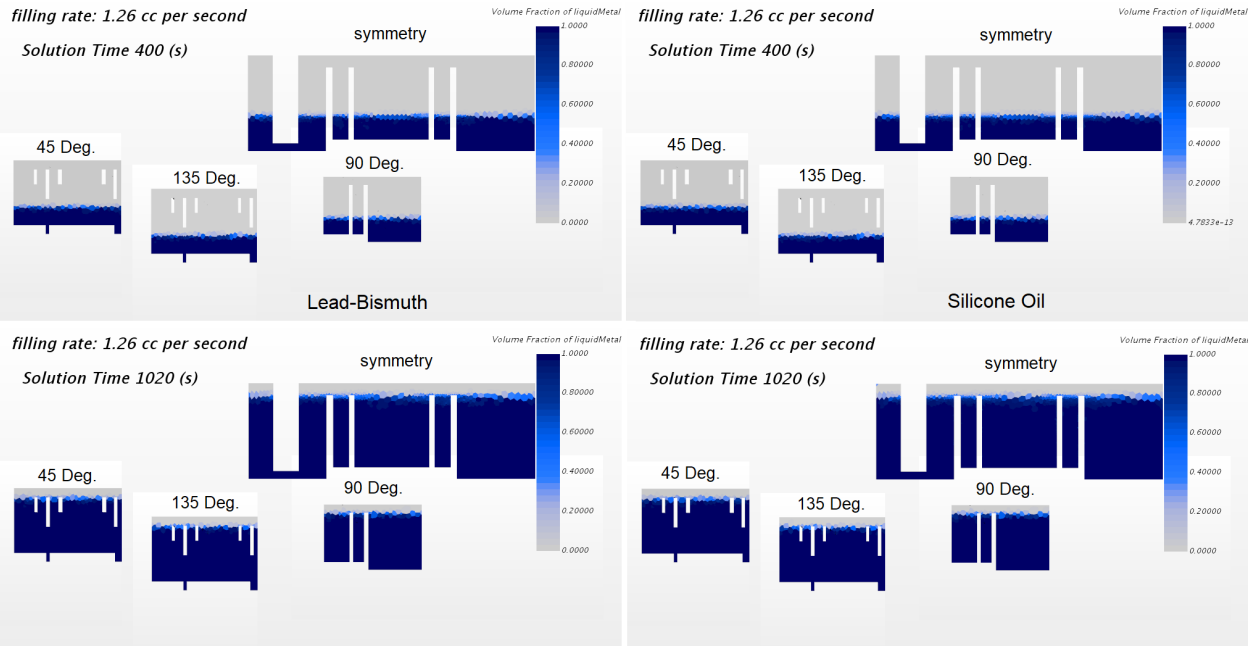

Figure 5. Liquid Levels at 400 and 1,020 s (end) of Transient from Two Runs with Different Liquids (Left: Lead-Bismuth; Right: Silicone Oil), and Contours of Levels at Several Sections of the Mouse Hole Region (Symmetry, 45-, 90-, and 135-Degree Cross Planes).

Even though the silicone oil density is much lower, it allows for the liquid to level off and to smoothly cover the entire region. The level velocity of 4.2 mm/min is such that the viscosity/density combination of the liquids does not affect the filling process. A detailed examination of the plotted sections does not show the presence of any voids. The same is confirmed by the overall volume balance, which is controlled during the simulation.

An isometric view of the simulated section is shown in Figure 6. The top wall and the symmetry planes are removed for better visibility inside the domain. The top part, as seen in Figure 5. , is added to the model to make the outlet pressure equal for all parallel cells. The DPC is designed so that each individual fuel bundle is confined in a separate shroud (cell). The cell walls do not allow for cross flow in the canister. The parallel cells are formed just above the mouse hole region, and the mouse holes are the only flow passage that permits the liquid to enter the fuel bundle cells. In order to properly simulate the filling of these individual cells, an extra volume is artificially added on top of this section to connect the parallel cells. This volume is not filled and does not affect the overall filling time or mass balance.

The views in Figure 6. provide another look at the filling process in the mouse hole region of the canister. This is the region where the bundle shrouds interconnect. The view on the left in Figure 6. shows an early stage of filling in which the central part is still not flooded. The liquid initially propagates on the circumference around the outside wall before entering the central area. Even though that space is narrow, the liquid can freely penetrate the space and distribute evenly in the remainder of the domain. The right view in Figure 6. shows a later stage of the filling in which the mouse holes are partially filled. By observing the levels in different cells, one can conclude that the process is very smooth, and the level rises evenly in all cells. Although the resolution of the model is quite low (to keep the compute time short), the numerical scheme used (high resolution level tracking) maintains the level within 1–2 grid elements. No numerical diffusion is observed due to the second order upwind scheme used to run the simulations. Note that the interface between the gas and liquid cannot be sharper than one element (the liquid boundary to match the element boundary) because the VOF method treats the liquid as a fraction of the total fluid, and as soon the level crosses the element boundary, the void fraction in the same element starts to increase

and varies from 0–1 before the element is completely filled. This explains the different color of gradient in the elements near the level.

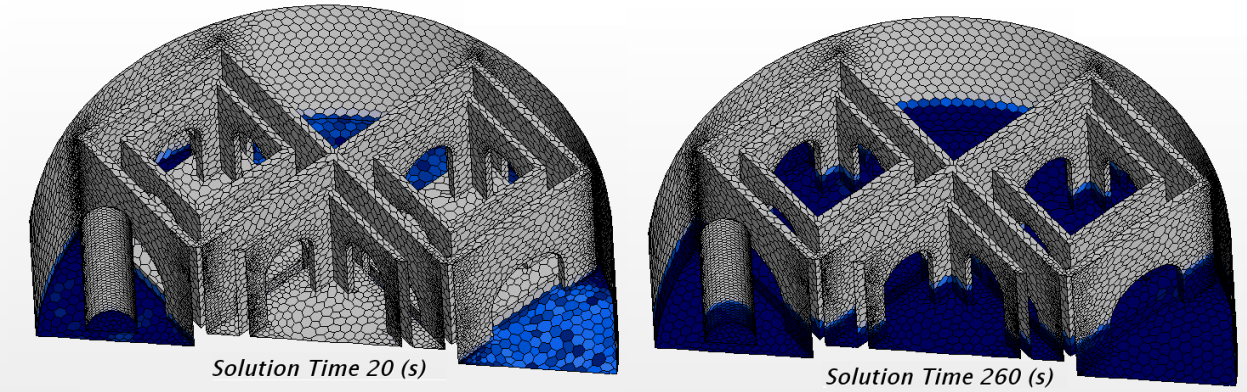

Figure 6. Liquid Content during Filling of the Mouse Hole Region at 20 and 260 s. Total Filling Time = 1,040 s; the Computational Grid is Also Shown.

An important aspect of the filling calculations is the conservativeness of the solution. The relatively coarse domain discretization poses questions about the solution's accuracy. To address these questions, a control of the mass in the system is established during the time advancement. The result is plotted in Figure 7. for three of the test liquids (Pb-Bi, Si-oil, Hg), and it shows that the error varies within 1.5%. In the simulation, the model fills for 1,040 s while the actual filling time is 1,024 s. The error tends to increase toward the second half of the process, which will be investigated in the future. The error could be due to the grid becoming larger in the space over the mouse holes. Usually, the element size is driven by the geometry features, and to resolve small details, more elements are used. Once details such as the mouse holes are meshed, the grid elements become larger in the spaces over the mouse holes. This may be increasing the error, but it remains within practical limits. In view of the long practical filling times, such a small difference is considered acceptable.

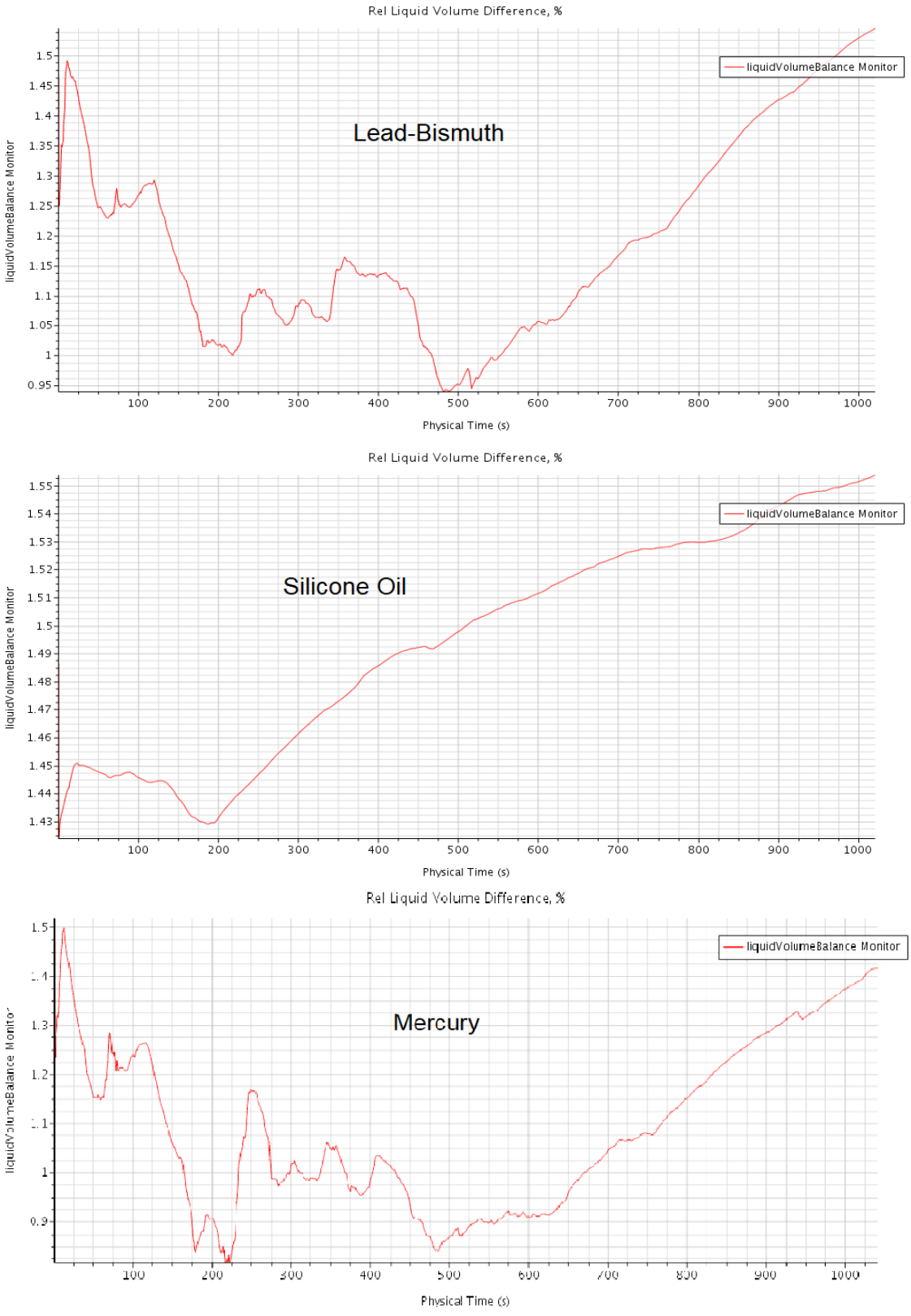

Figure 7. Mass Error Evolution during Filling of the Mouse Holes Region with Pb-Bi (Left), Silicone Oil (Center), and Mercury (Right).

2.2 Lower Grid Filling Simulation (In Progress)

As shown in Figure 4, upstream of the mouse holes, there is a section (~180 mm) where the geometry does not change. This section contains the liquid in the fuel assemblies' supports. The fuel assemblies are placed in the canister on rectangular supports that separate them from the canister floor. After filling of the mouse holes has been successfully demonstrated, there is no need to carry the numerical solution in that region because no new geometry features exist. Instead, this section is skipped by shortening the domain to save computing time. The level, which is computed in the region below (mouse holes), is transposed as an input condition, assuming it has the same topology. The rationale is based on the fact that no specific features of the level are observed, like moving or standing waves, substantial radial convection, etc., which would invalidate the above assumption. The liquid front propagates in all cells with the same velocity. Technically, this is accomplished by mapping data between nonconformal domains, which is challenging in CFD computing, but it can be done. This approach is followed in the present analyses.

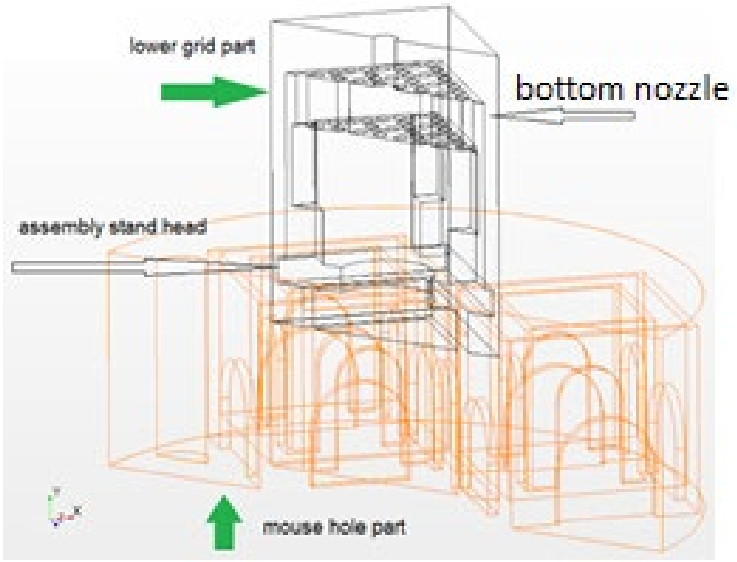

Figure 8. Lower Grid and Its Relative Position to the Mouse Hole Region Used in the Simulation. The Important Features of That Section Are Indicated.

The simulated section is shown in Figure 4. This bottom nozzle includes several small holes that, in the reactor design, were originally meant to provide more even flow distribution at the bundle's inlet. These holes may pose a problem in the filling process and will require special attention. The modeled section also includes the upper part of the assembly stand and the transition region. It is part of one of the five 5 × 5 bundles. As mentioned before, the bundle cells (shrouds) permit the domain to be further decomposed and simplified by simulating only one of the five bundles (because they form identical parallel channels).

More detail about these components and their relative positioning is shown in Figure 8. The mouse hole region is shown with different colors to distinguish the components. The section has an overall height of 113 mm. It is set to overlap the mouse hole region, with 15 mm to allow for data mapping. The overlap is shown in Figure 8. The lower grid section is meshed with about 100,000 elements. When compared to the mouse hole region, this increased number of elements is about 5 times larger and has 45,000 elements. This is caused by the holes in the lower assembly grid.

To provide continuity of the filling process, two variables from an existing solution in the mouse hole region must be mapped to the lower grid region. One of them is the current level, expressed as liquid

volumetric content (fraction of total fluid). The level is usually spread across at least three layers of elements, which determines the mapped domain. Figure 9 (below) shows the outcome after the mapping is performed. A partial level of data only in the central cell is mapped to the lower grid region. It covers part of the bundle support fluid volume just below the lower grid. The volume of this initial liquid is 15 cc, and it must be accounted for in the over-volume balance during the simulation. The computational mesh is demonstrated in Figure 9. (below), with a zoom into the lower grid holes. The geometry is captured in full detail, resulting in an increased element count.

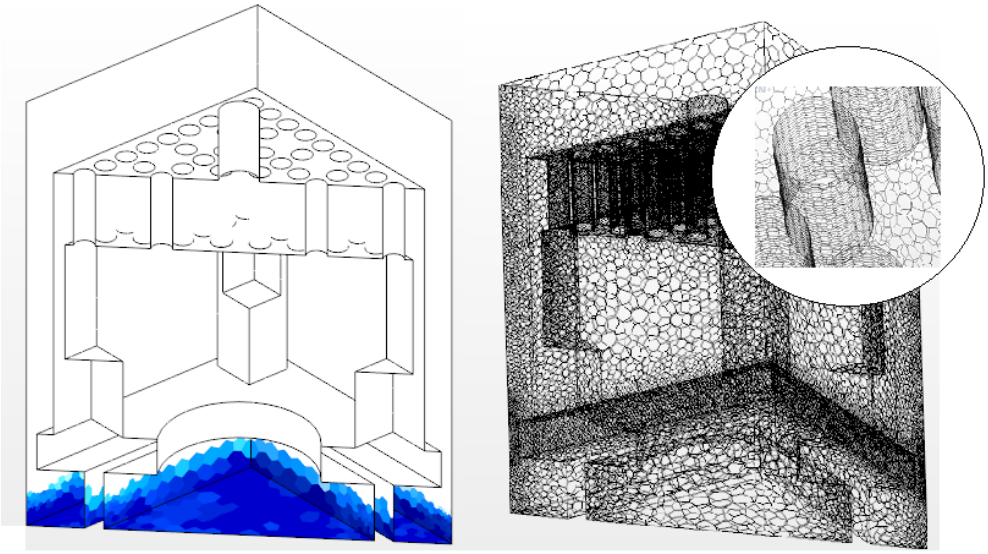

Figure 9. Initial Liquid Fraction as Mapped from the Mouse Hole Region (Left), and Computational Mesh of the Lower Grid Region with a Zoom into the Hole Area's Mesh (Right).

The second variable that must be transferred from the previous solution is the velocity vector at the inlet of the new section. A close examination of velocity vectors in a plane just above the mouse holes (Figure 10.) shows a random high frequency distribution of instantaneous velocities. The dominant magnitude is around 0.05 m/s, with no preferential direction. The insert window in Figure 10. enlarges the velocities in the mapped area and shows the computational grid. Such a velocity profile is calculated by the viscous solution when no ensemble time averaging of velocity is performed. The difference between the instantaneous velocity and the axial average velocity (~4mm/min) indicates that a small-scale turbulence is computed in a general laminar flow. Further examination of the velocity contours in the mouse hole region does not indicate formation of eddies, indicating that the flow is not turbulent. The Re numbers for that region, based on the level velocity and typical length scales (~70mm), are ~15. This finding requires more attention and further analysis of the origin of these fluctuations, which are most likely numeric.

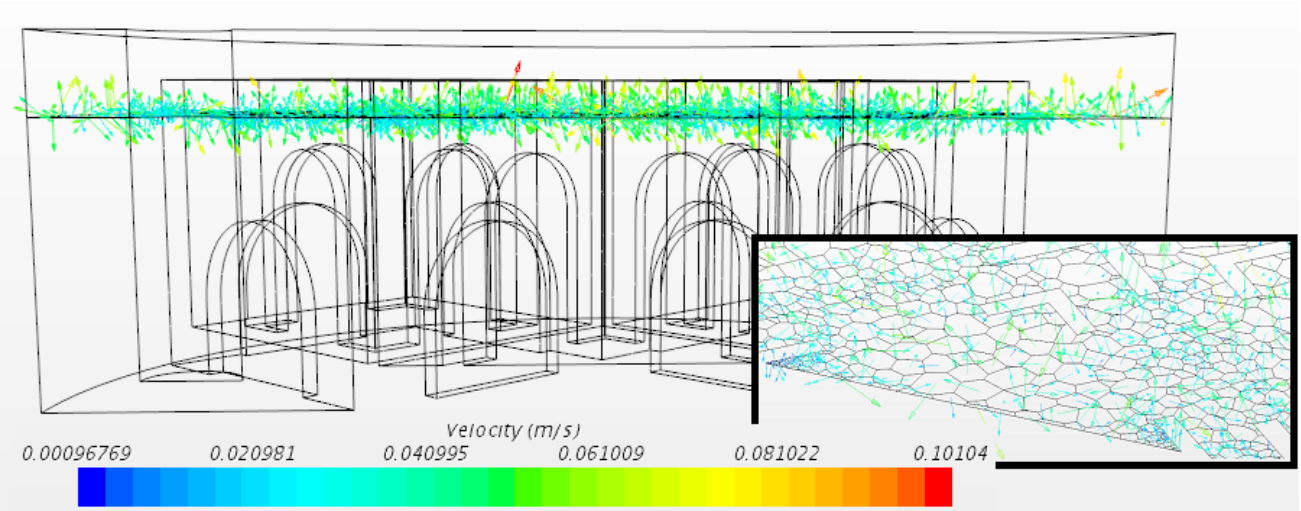

Figure 10. Velocity Vectors of the Advancing Liquid Level on a Plane Just above the Mouse Holes. The Random Fluctuation of Liquid is Noticeable, with no Preferential Direction. The Insert Shows the Mesh and the Velocities in the Mapped Region.

Based on the results discussed above, instantaneous velocities are not suitable as a boundary condition for the lower grid region unless they are time averaged. Instead of time averaging, the velocity at the inlet section of the lower grid region is calculated after the filling rate for the same region is calculated. Additional data are needed to perform this calculation, as summarized in Table 2.

Table 2. Geometry data for the bottom nozzle section and for the half symmetry model with the same axial elevations.

Parameter	Value
Volume of lower grid region	224 cubic centimeters (cc)
Axial height of lower grid region	113 mm
Inlet flow area of lower grid region	2137 mm^2
Volume 113 mm tall	2047.8 cc
Overall filling rate for the entire model	1.26 cc/s

The approach is based on calculating the overall time for filling a section of the entire geometry with the same axial marks as the lower grid section: 113 mm. The filling time of the entire geometry with 113 mm height = volume (local) of entire geometry / overall filling rate:

$$T_{total} = 2047.8/1.26 = 1625 \text{ s} \quad (5)$$

If the same filling time is valid for the lower grid section of the geometry, then a part specific filling rate can be calculated:

$$\text{Filling rate (lower grid)} = \text{volume of lower grid} / T_{total} = 224 / 1625 = 0.138 \text{ cc/s} \quad (6)$$

Once the part-specific filling rate is known, the inlet velocity is calculated:

$$\text{Inlet velocity for the lower grid section} = \text{Filling rate (lower grid)} / \text{inlet flow area} = 0.138 / 2137 = 6.45\text{E-}5 \text{ m/s} \quad (7)$$

This velocity is slightly lower than the level advancement velocity of 4.2 mm/min (7.0E-5 m/s) mentioned before. The difference appears because the flow area in the lower grid section is smaller than the average flow area in the same section of the entire geometry. The inlet velocity is applied to the inlet geometry of the lower grid section together with mapping the level from the mouse hole section. These two initial conditions are sufficient to perform the calculations. The mapping is successfully accomplished following a code-specific procedure, and the analyses runs will be initiated soon.

The computational runs are successfully started and are under way at the time of this writing. They are being executed on 96 cores (three nodes 32 cores each). The first 500 s of the transient are calculated. The level progresses smoothly as in the previous DPC section (mouse holes) without any anomalies. The liquid level has not reached the lower grid area and it is still in the transitional region between the assembly stands/spacers and the lower grid. Four snapshots of the entire lower grid section showing the level advancement are plotted in Figure 11. The grid hole area is clearly visible above the current level position.

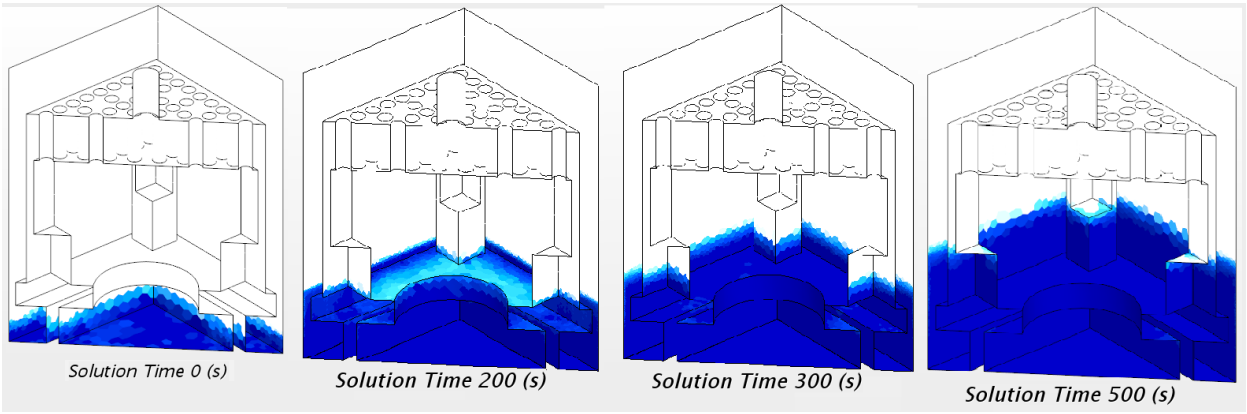

Figure 11. Evolution of the Level in the Lower Grid Section of the Model during the First 500 s of Transient.

In terms of resolution, the holes are the denser part of the domain and will require more computing time. The period of 500 s is computed for about 19 hours of CPU time per processor, or with about 0.2 hour of clock time per second of real process. At this speed, the entire filling simulation should be completed within a week.

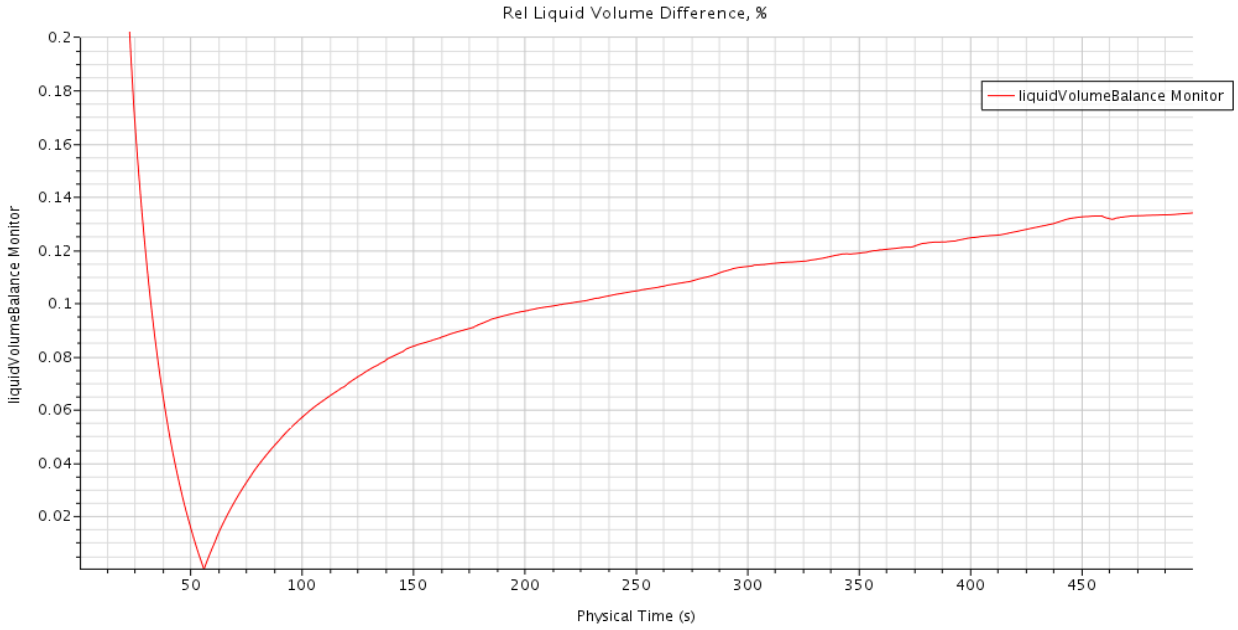

Figure 12. Mass Error Monitor. The Total Mass in the System is Constantly Evaluated and Compared to an Ideal Process.

The mass error is continuously being monitored (Figure 12). The current value is about 0.14%, which when converted to real volume yields 0.3 cm^3; it tends to stabilize at this level. This number indicates a very good solution convergence and accurate spatial discretization.

To allow for axial tracking of the filing process and identification of eventual voids, several cross sections of the domain are plotted in Figure 13. They are taken in the symmetry plane (mid-section) and at 45, 90, and 135 degrees sections. The information from these plots shows an even level progression and no void formation. The most critical area for voids is the grid, and the solution has not yet reached that location. The section that has already been filled is quite free of obstruction, as the flow enters by a central opening with a large area which does not present a challenge.

The simulations continue, and without any further complications, they are expected to complete in a week, depending on the load on the computing cluster.

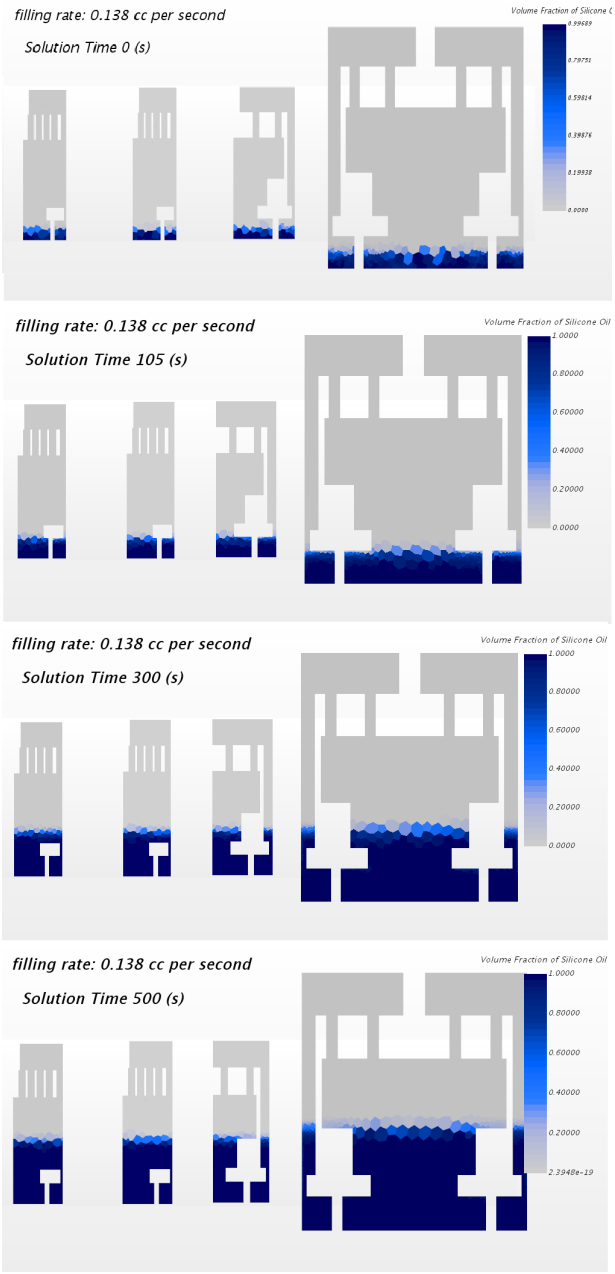

Figure 13. Filling of Lower Grid Region, Sectional Liquid Fraction Plots, Showing the Volume of the Lower Grid Filled at Different Time Instances. The Calculated Period Covers the Transition between the Stand and the Grid Entrance Region.

2.3 Drain Pipe Analysis and Modeling Approach (Not Started Yet)

The drain pipe analysis and modeling evaluations have not been initiated yet because the filling simulations are receiving higher priority. The information presented here is preliminary should be considered an introduction to the problem.

One consideration is to evaluate the possibility of filling the canister through the drain pipe. Each DPC is equipped with a drain pipe and a vent port of the same size (ID 1.25 in.). The drain pipe stretches from the top of the canister to the bottom, so it has the same length as the canister. The pipe is about 4.26 m (14 ft.)

long. While there is no strict requirement for how much time the filling of a single canister should take, the drain pipe's capacity to deliver a steady flow of liquid metal to the canister may be the limiting factor for the filling time and could be the component that will define this time. In the simulations, a filling time of 17 hours is assumed based on a filling rate of 100 ml/s. The assumed free canister volume is 6 m^3.

Extensive research has been conducted on flows in vertical pipes. In the past, intrusive methods such as hot wire anemometry were used, but more recent experimental works use non-intrusive techniques such as laser doppler velocimetry (LDV), photochromic dye tracing (PDT), confocal chromatic imaging (CCI), or particle image velocimetry (PIV). Two recent experimental and theoretical studies by Zadrazil and Markides [8] and by Padmanaban [9] address vertical pipe flows, mainly of water. When the pipe entrance is not obstructed by liquid (as in a pipe draining a tank) but is left open to the air or a gas atmosphere, the flow that develops in the pipe is a two-phase annular flow. In this type of flow, the liquid flows steadily on the pipe walls, forming an annular film. The core of the flow is gaseous and is typically stagnant. Some experiments consider co- or counter-current gas flows [9], but they are outside the initial scope of this work. Co- or counter-current gas flows are of interest for the canister filling because they would provide a means to control the flow rate without chocking the pipe. The term *chocking* is used here to indicate a regime in which the entire pipe area can become fluidized, and there would be no free flow of gas in the pipe. These evaluations will initially be assumed that this type of regime is unwanted, as it would impede the steadiness of canister filling by creating flow pulses, shocks (hydro) or other hydraulic phenomena. This could damage canister structures or disrupt the filling process due to the high gravity effect of liquid metals, which have densities approximately 10 times greater than that of water. This option will be further reevaluated during this study and may be revised. Figure 11 presents a typical drain port design.

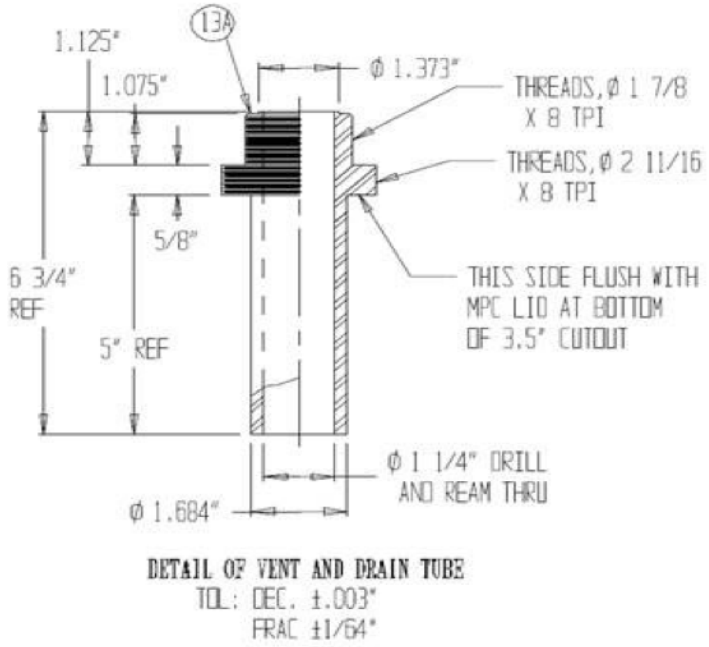

Figure 14. Drawing of the Drain Port Showing the Side of the Opening [5].

The Nusselt film theory can be used as a starting point in these analyses because it gives a good first order approximation to the main flow characteristics. It is based on the assumption that a steady liquid film forms on the pipe inner wall (or other structure wall) which is one dimensional (only in axial direction) and the film flow is laminar. Under such circumstances, the wall shear stress balances (in a steady condition, when the axial velocity is constant) with the force of gravity. This can be written as

$\frac{\partial \tau_{yz}}{\partial y} = -\rho g$, where τ is the shear stress in z (axial) and y (normal to the wall) direction; g is gravity; and ρ is the liquid density. Normally, the z-y shear component can be presented as $\tau_{yz} = \mu(\frac{\partial W}{\partial y} + \frac{\partial V}{\partial z})$, with the second term in one dimensional flow is given by $\frac{\partial V}{\partial z} = 0$. Thus, the final equation that defines the film velocity becomes:

$$\mu \frac{d}{dy}\left(\frac{dW}{dy}\right) = -\rho g, \tag{8}$$

where W is the axial and V is the radial velocity component. In one dimensional formulation, only W is non- zero. The above equation can be integrated with the following boundary conditions: W =0 at the wall, and $\frac{\partial W}{\partial y} = 0$ at the film thickness of y = δ. The result gives the velocity distribution in the film:

$$W(y) = \frac{g}{\nu}\left(\delta . y - \frac{y^2}{2}\right), \tag{9}$$

where ν is the liquid kinematic viscosity and δ is the film thickness.

Assuming further a flat film (not exactly the same that forms in a circular pipe), the flow rate of liquid per unit width of film can be calculated by integrating the following expression over the film thickness:

$$q = \int_0^{\delta} w(y)dy\,. \tag{10}$$

The result of the above integration provides a simple relation between the film thickness and the volumetric flow rate:

$$\delta = \left(\frac{3\nu q}{g}\right)^{\frac{1}{3}}. \tag{11}$$

This relation can be used as a first approximation for evaluating the film thickness that forms in laminar conditions in a gravity driven flow. To make that relationship applicable when the flow rate Q (m^3/s) is known, an additional assumption for the film width is necessary. In case of very thin films, the film width of a film flowing on the inner pipe wall, will be very close to the pipe perimeter. In such condition, the relation between Q and q is given by $q = Q/\pi D$, (m^2/s), where D – is the pipe diameter.

With the help of the above relation the film thickness can be finally evaluated as:

$$\delta = \left(\frac{3\nu Q}{\pi g D}\right)^{\frac{1}{3}}. \tag{12}$$

The non-dimensional parameter that characterizes the flow of liquid films is the Reynolds number *(Re)*. Traditionally in the liquid film flow theory, the *Re* number is defined in two different ways: by the Nusselt velocity W_{Nu}, or by the superficial velocity W_{sl}. The Nusselt velocity is formulated directly from the flow rate defined above:

$$W_{Nu} = \frac{q}{\delta} = \frac{\frac{g}{\nu}\delta^2}{3}. \tag{13}$$

The definition of the *Re* number is based on the Nusselt velocity and the film thickness and is given by:

$$Re_{Nu} = \frac{W_{Nu}\delta}{\nu} = \frac{g\delta^3}{3\nu^2}. \tag{14}$$

The formula allows the film thickness to be calculated by knowing the Nusselt Reynolds number.

Substituting the film thickness in the above, leads to a relatively simple relation between the *Re* number and the flow rate:

$$Re_{Nu} = \frac{q}{\nu} = \frac{Q}{\pi \nu D}. \quad (15)$$

For Lead-Bismuth (Pb-Bi) eutectic (ν = *3.039E-7 m^2/s*) and for the chosen flow rate of *100 ml/s (Q = 1.0E-4 m^3/s)*, and for the size of the drain line *(ID = 1.25" = 0.03175 m)*, the Nusselt Re number is: Re_{Nu} *= 3298*. The Nusselt film thickness can also be calculated, using the above formulas for Pb-Bi: δ *= (3.3.039E-7.1.0E-4/π/9.81/3.175E-2) ^1/3 = 0.45 mm*. The corresponding Nusselt velocity can be used as a measure of some average film velocity. It is formulated above and is calculated below:

$$W_{Nu} = \frac{q}{\delta} = \frac{Q}{\pi D \delta} = \frac{1.e-4}{\pi\ 0.03175\ 0.45e-3} = 2.23\frac{m}{s}. \quad (16)$$

The second method to define the *Re* number is by the superficial velocity. The superficial velocity is the velocity of liquid if occupying the entire pipe and is given by: $W_{sv} = 4Q/\pi/D^2$. The *Re* number is then defined based on that velocity and the pipe diameter: $Re_{sv} = W_{sv}.D/\nu = 4Q/\pi/D/\nu \rightarrow Re_{sv} = 13{,}195.$

The flow characterization based on the Nusselt theory helps to obtain a first guess for the expected flow behavior in the drain pipe. Due to the high gravity of the liquid metals, the Re numbers are 2-3 times higher than that of water. The resulting laminar flow film thicknesses are small (thin films) because of the same reason. It is highly expected that the flows will develop unsteady turbulent patterns. Therefore, the above introduced method won't be sufficient for correct prediction of the film motion. It is possible the problem to be approached numerically by performing CFD analyses of turbulent liquid films. The CFD is superior to the simple laminar one-dimensional theory, because it can provide multidimensional solution of the turbulent liquid gas interface.

In this short introduction to vertical free falling liquid films only water experiments are briefly reviewed. One of them is [8], where tests on a 3m long (ID 32.4 mm) pipe were performed. The pipe diameter and length are almost the same as those of the DPC drain pipes. Two high resolution techniques were employed for flow characterization: PTV/PIV (particle tracking velocimetry) and PLIF (planar laser induced fluorescence). Both methods allow for accurate velocity measurements (instantaneous), gas liquid interface capturing, identification of wave appearance and propagation, and recirculation zones formation. The measurements were taken on a test section 72D from the pipe inlet. The test setup allows co-current gas to be injected in the core of the flow. The review is limited to the tests with zero gas flows. They cover a range of ReNu between 306 – 1532, which is substantially lower than the range expected during the DPC filing.

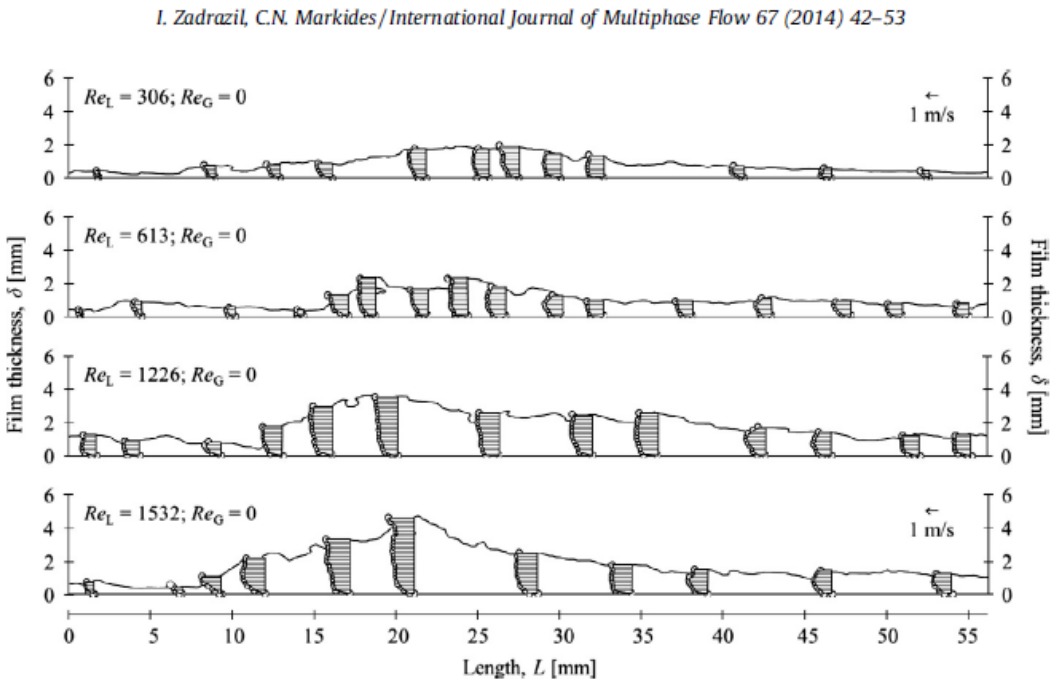

Figure 15. Liquid Film Instantaneous Velocities Showing Appearance of Waves. The Waves Grow with the *Re* Number.

A detailed image from CD-Adapco [6] shows the film thickness and the instantaneous velocities (Figure 15). For $Re_{Nu}>300$, waves start to appear and grow as the *Re* number increases. The wave velocity was also measured, which for the studied range of *Re* was around 1.5 m/s. It is noticeable that the mass transport is dominated by the wave size and not by the speed. The flow structure is defined by some basic substrate thickness (a constant thin portion of the film) and the waves traveling in this substrate. Recirculation zones are also seen in the wave crests; these are an indication of turbulent flow.

The flow visualization method used in Zadrazil and Markides [8] allowed the film velocities to be time averaged and accurately measured. Figure 16 is likely the most representative plot (also from Zadrazil and Markides) for zero gas flow, which is of interest in this study. The figure illustrates the mean film velocity profiles. The highest *Re* number results demonstrate that the film thickness stretches to 20% of the pipe's radius (~3.24 mm). These film thicknesses are in the waves. The substrate film thickness is marked with empty signs on the velocity plots. It indicates thicknesses of ~0.05R, or ~0.8 mm. Because the *Re* is about two times lower than in the case of Pb-Bi, the film's measured thickness is almost two times higher than the estimate given above for Pb-Bi. This observation points to a different flow structure that is characterized with thinner and faster films. The same conclusion is supported by comparing the profiles in Figure 16 with the estimate for the Nusselt velocity (2.23 m/s) of the Pb-Bi film. For the base film thickness (Figure 16), the velocities are between 1–1.5 m/s, and they grow slightly in the wave's crest. Apparently the time averaging does not capture the instantaneous wave velocities, which creates a perception that the waves travel with the same velocity as the film (substrate), or almost the same (~20% faster). This observation must be carefully addressed to avoid reaching a wrong conclusion. The paper by Zadrazil and Markides [8] also provides data for CFD model validation, because turbulence-related properties such as kinetic energy or Reynolds stresses are calculated from the recorded instantaneous velocity field.

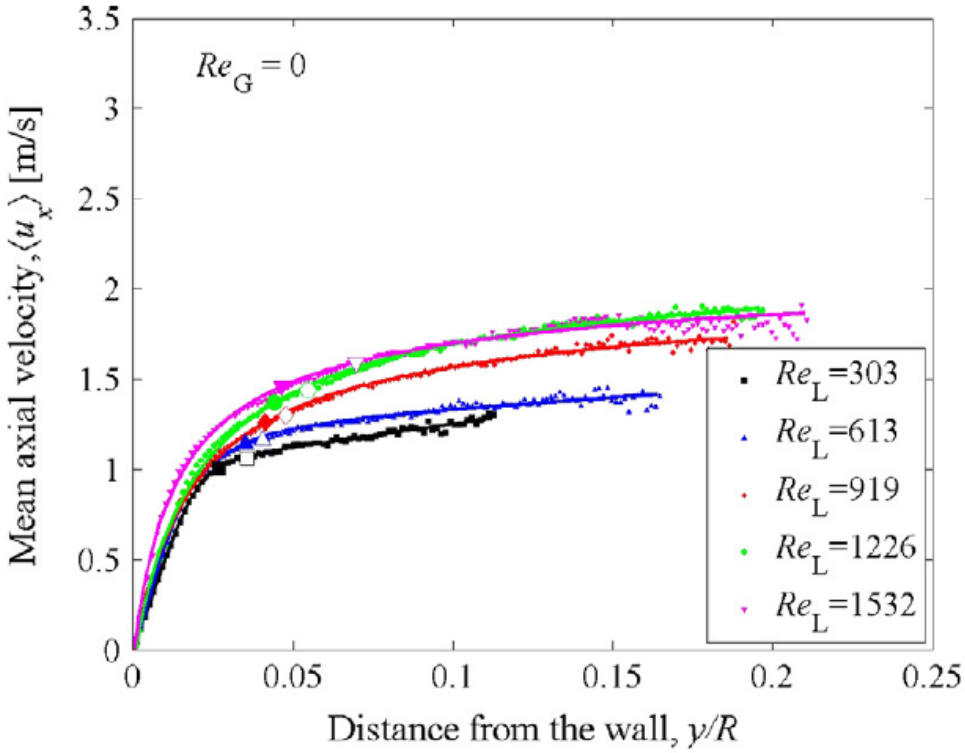

Figure 16. Axial Mean (Time Average) Velocity Profiles from Zadrazil and Markides [8] for Free-Falling Liquid Films (No Co-Current Gas Flow). The Substrate and the Average Film Thicknesses are Shown with Solid and Hollow Markers on Each Corresponding Plot.

Another interesting work is presented in Padmanaban's thesis [9]. This work did not employ such high - resolution visualization technique as used by Zadrazil and Markides [8], but the experiments were run up to higher *Re* numbers, close to or even exceeding those that are targeted in the DPC filling study. A straight vertical pipe with an ID of 1 inch (0.0254 m) and length of 4 m served as the test section. Photographs were made of the falling free films of water. The images were corrected to allow for better contrast in the wave area. Selected liquid film photos are shown in Figure 17 for three regimes with *Re* numbers of 13,348; 18,208 and 23,696. The regimes are selected to match (first one with *Re=13,348)* or to exceed the expected DPC filling *Re* numbers. The white arrows in Figure 17 indicate the region where the film flows next to the wall, to the waved area over the film, and to the gas bubbles. Annotations to the arrows provide more detail about the objects they specify.

The left image shows a liquid film with no gas, a wavy structure over the film (substrate), and a gas core with some liquid droplets. It seems that the film thickness is on the limit of beginning to disintegrate. The next image (center) has almost no gas core. The waves have grown large enough to block the entire cross section of the pipe. The flow regime starts to transition from annular film to churn-like flow in which the core is a mixture of gas and liquid. The right image demonstrates the breakup of the film and a falling flow of mixed gas and liquid. Gas is entrained in the liquid, and the liquid is entrained in the gas core. The liquid film is difficult to distinguish. This occurs at *Re* less than two times higher than the *Re* of interest in the filling analyses.

Based on this information, it can be concluded that the initially selected filling rate of 100ml/s will produce a turbulent film with large waves contributing substantially to the mass transport. The flow regime is close to a transitional mixed liquid-gas regime, which at this time is considered questionable for delivering a steady flow of liquid to the canister.

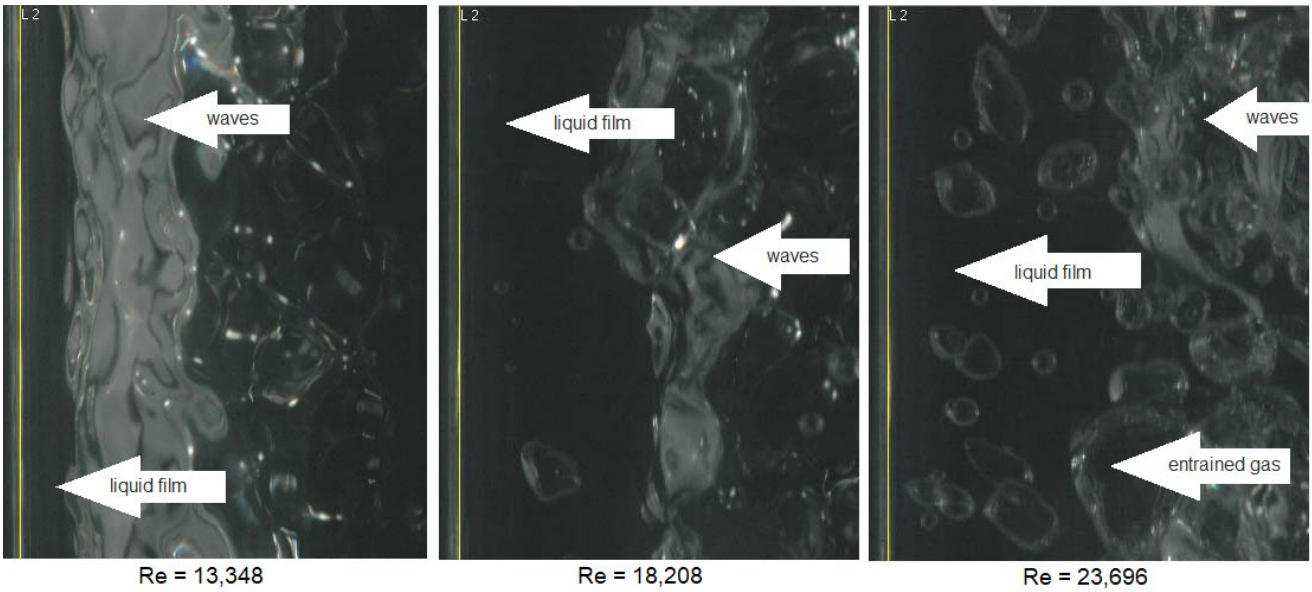

Figure 17. Photos of Free-Falling Films [9]. Only the Left Half of a Cross Sectional Area of the Pipe is Shown. The Wall is on the Far Left, and the Film is the Dark Area Next to the Wall. Gray-Colored Regions Show the Waves, and the Far-Right Image Shows the Entrained Gas.

Besides capturing the film topography, Padmanaban [9] provides measurements of the turbulent mean film thickness. The results are based on statistical processing of more than 40,000 images for each of the different flow rates. The data are correlated in analogy with the film's thickness (δ) from the Nusselt theory. To compare with other data, these data are nondimensionalized with a factor of $(\nu^2/g)^{1/3}$. The result is plotted in Figure 18. The *Re* number in Figure 18 is four times smaller than that used in this work due to different formulation (*Re = 13.195/4 = 3300).*

The nondimensional film thickness for this *Re* is *~35* (from Figure 18). Applying the factor given above, the dimensional film thickness for Pb-Bi can be calculated: *δ = 35(3.039E-14/9.81)^1/3 = 0.51 mm.*

The result is about 12% different from the Nusselt thickness of *0.45mm* given above. The difference is due to the wave formation that is captured in the experimental studies, but once averaged, it produces almost the same thickness. The average film thickness is only one of the flow characteristics. Another equally important characteristic is the wave height, which has only been measured in more recent works in which advanced visualization techniques were employed.

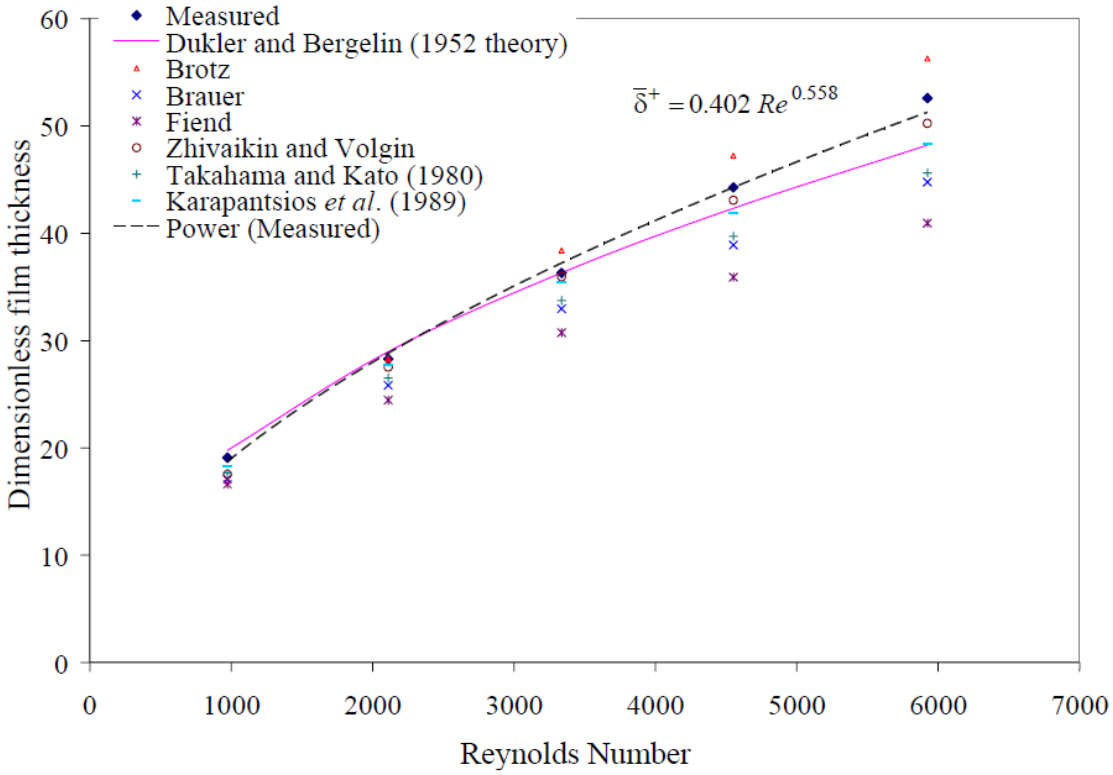

Figure 18. Dimensionless Film Thickness in Function of Re Number [9] for Comparison with Previous Experimental and Theoretical Data.

The limited review of existing data for free-falling liquid films in circular pipes reveals several useful findings.

1. There is an abundance of data for liquid films in pipes for low *Re* number flows. Data are more limited for high *Re* turbulent films because neither the theoretical models nor the experiments are easy to conduct. Most of the industrial applications involve turbulent flows, including the DPC-filling problem.
2. Within the scope of this initial work, no data were found for falling films of liquid metals. The search will continue in the future; however, it seems that experimenting with annular liquid-gas flows might be advisable in the filling demonstration project. The objective of such experimentation will prove that a steady, stable, liquid metal (Pb, Hg, Pb-Bi) film can be created and maintained for hours during the DPC filling.
3. Experimenting with liquid metals may pose new questions and may require new visualization methods, because, unlike materials most used for testing liquids, the metals are not transparent. Metals have much higher surface tension (about 6 times higher than water) than most liquids used for testing in most experiments. In the work of Kapitza [10], the surface tension is analyzed, and a parameter is introduced—$\gamma = \sigma / \rho\nu^{4/3} g^{1/3}$—where σ is surface tension. It is shown that the surface tension has a strong effect of the formation of waves in the film. It is expected that the liquid metal will have different film topology and perhaps different thicknesses for the same *Re* numbers.
4. Another aspect to be addressed is the drain pipe geometry and positioning in the canister. In the experiments with falling films, the pipes are well aligned and positioned perfectly vertical. In a real situation inside the canister, the drain pipe may not be vertical or even straight due to aging or other thermal or structural factors. Evaluations of the effect of pipe position and geometry on the formed liquid film might be necessary.

This initial introduction to the flow phenomena in circular pipes with free-falling liquid-gas films indicates that more studies are necessary in order to draw conclusions about using the canister drain pipe for filling with liquid metals.

2.4 Planned DPC Drain Pipe Flow Experiment

As discussed above, it is imperative to thoroughly understand the filler materials that flow through a pipe. A separate computational simulation and experiment are necessary to understand any unforeseen issue of filling a DPC using a drain pipe. This experiment will inform decision making regarding filling DPCs using a drain pipe. Due to the high specific gravity of metals, filling by creating a liquid film on the pipe walls is conceivable. The resultant flow regime is two-phase, annular. If properly organized and controlled, the filling could be smooth, continuous, without pulses, vibrations, or other hydraulic effects that may compromise the entire filling process.

The literature includes many experimental and analytical studies of vertical annular flows in pipes. However, most of these have been conducted using water or other light liquids. It is difficult to find any existing literature describing studies using liquid metals. Liquid metals differ from water in two major properties—density and surface tension—two extremely important properties when considering the annular film that develops on the pipe's wall. Experimenting with liquid metals can prove the feasibility of filling through the drain pipe. Simulations (CFD) can be carried out along with the tests to compliment the assessment and to allow for scaling the problem to a real DPC.

Most of the metals are solid at normal (room) conditions. Bringing the metals into liquid state for experimentation would be expensive. To avoid this expense, mercury can be used as a surrogate metal. Mercury is heavier than most metals and has comparable surface tension, which qualifies it as an ideal surrogate. ORNL has already developed an infrastructure for experimenting with mercury which can easily be leveraged for this type of testing.

Average liquid film thickness and topology are important for detailed understanding and simulation of annular film flow of liquid metal in vertical pipes. The existing models and correlations either have large relative errors or narrow application ranges. Therefore, a new set of experiments with mercury is being planned to provide greater understanding of the process and to complement the existing knowledge base of annular vertical pipe flows. The proposed data collection will include pressure, liquid and gas velocities, liquid film thickness, effect of viscosity, etc. Previous studies indicate that the film thickness is a function of Reynolds and Weber numbers for both liquid and gas. The collected flow regime data will be used mainly to establish limits for maximum and minimum liquid filling rates in the system. Analytical models will be developed and benchmarked along with the experiments.

2.4.1 Film Thickness Measurement Technique

Unfortunately, liquid metals are opaque and reflective, and light methods will not be applicable for flow visualization. Instead, the film's thickness can be measured using a conductivity-based technique. For a conducting liquid (e.g., mercury), the liquid film's thickness is proportional to the conductance of the film, whereas the droplet-laden gas core is not. Therefore, the approach is to impose an electrical potential between a pair of electrodes in contact with the liquid film and measure the resulting current, which is a function of the conductance of the film, hence of its thickness. This technique has been used extensively [11, 12].

A cluster of four film thickness sensors is shown in Figure 19(a). The sensor consists of one "transmitter" ring electrode, 32 "receiver" island electrodes equally spaced around the circumference, and one insulation ring. The ring and island electrodes are flush with the inner pipe wall, making the film thickness sensor nonintrusive. During the signal acquisition, the transmitter electrodes are activated successively by supplying them with a rectangular voltage pulse. For each transmitter activation, the resulting current is measured successively at the receiver electrodes in the corresponding unit. A full

cycle, which is necessary to activate all transmitters and to measure the current at all receivers, takes 0.2 ms. Therefore, the total measuring rate is 5 kHz, which is much higher than the physical phenomena observed in annular flow. The principle and the signal acquisition hardware are the same as those in the electrode-mesh sensor of Prasser et al. [13].

The sensor is calibrated experimentally using a static liquid film. It is made by inserting a nonconducting insert of known diameter into the sensor, mimicking the gas core, and filling the remaining volume between the sensor and the insert with mercury. A calibration curve is determined for each receiver with the fit-model. A typical example of a curve fit is shown in Figure 19(b). It shows that the sensitivity of the sensor decreases for increasing film thickness and that a film's thickness up to about 3.5×10^{-3} m can be measured with sufficient sensitivity.

The current measured film thickness at a receiver is a function of the film's conductance integrated over the control-volume in between the transmitter and receiver. Therefore, at each measurement location, a mean film thickness averaged over this control-volume is measured at each instant. This approach is intrinsic to the conductivity-based film thickness measurement technique and is also true for the conductivity-based measurements in the literature.

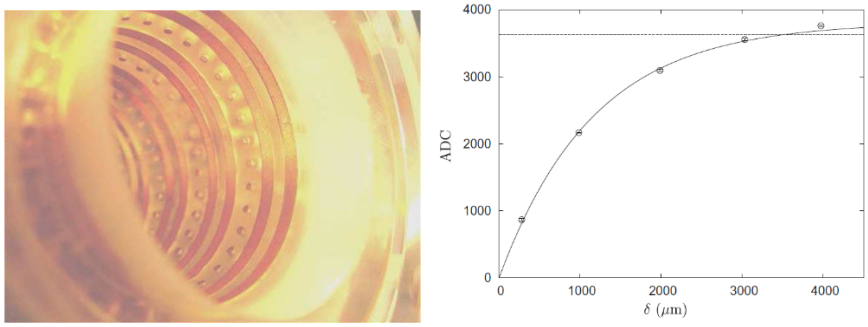

(a) (b)

Figure 19. (a) Photo of Film Thickness Sensor; Conductance is Measured between a Ring-Electrode and an Island-Electrode Flush within the Wall. (b) Typical Calibration Curve Using Stagnant Mercury Film.

2.4.2 ORNL Mercury Facility

The Target Test Facility (TTF) shown in Figure 20 is a full-scale Spallation Neutron Source (SNS)-prototypical mercury loop that was recently modified to accommodate a smaller test section using a reduced flow rate. The facility has an inventory of ~19,000 Kg of liquid mercury, and it can drive a maximum of 547 gpm using a variable frequency driver to control the loop's pump. The typical discharge shutoff pressure is 180 psig. The facility is enclosed in an isolated room that provides independent ventilation and a filter system that is able to remove mercury vapors and maintain safety levels inside the enclosure. This facility counts with mercury vapor monitors and alarms that monitor mercury vapor levels inside the enclosure and its surroundings. A team of trained personnel with extensive experience in mercury handling operates the loop.

A simple extension of the mercury loop configuration can be designed and built to experiment with a vertical pipe of the same size as the DPC drain pipe (4m, 1.25-inch ID). It will require some small modifications of the existing configuration and procurement of the necessary instrumentation. The existing data acquisition system can be used. This investment will be minimal compared to the initial investment in the existing mercury loop.

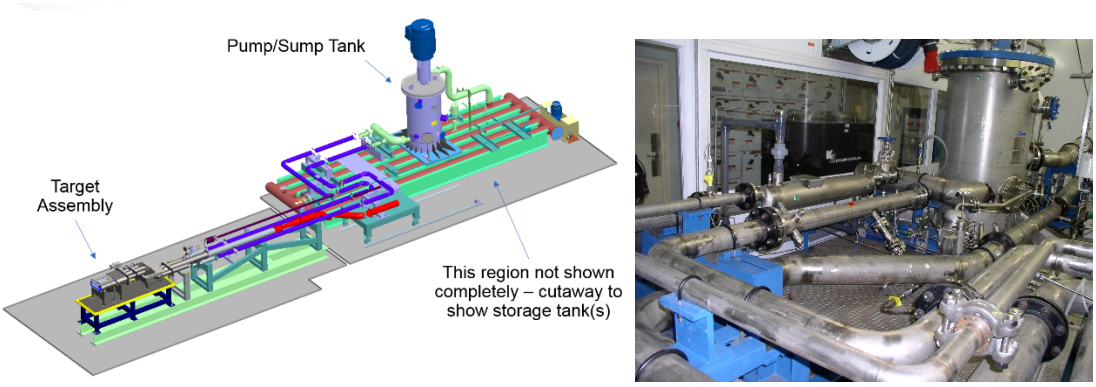

Figure 20. Target Test Facility (TTF) Mercury Loop.

2.5 Discussion

The filling simulations that have been performed on the lower region (mouse holes) of a prototypic DPC show successful filling of the inner space voids and smooth, even liquid level progression. Several liquid metals and surrogates are being tested as potential candidates for fillers. The problem requires intensive computing and is a good candidate for a high-performance computing application. Additionally, a pipe flow experiment to gain insight into filling a DPC using drain pipe has been discussed. Future work includes filling the upper regions of the canister, assessing options for filling through the drain pipe, and model validation on lab-scale experiments.

This page is intentionally left blank.

3. INITIAL FILLING DEMONSTRATION

The objective of experimental testing is to validate the computational models designed to simulate the filling process. The scope of the experimental studies documented in this report is to provide validation for single physics, or unit testing of flow simulation to determine injectability, void filling, filling time, filling method (gravity vs. pump), etc. In the subsequent phases of this work, other phenomena, such as the thermodynamic process of phase change behavior and heat transfer, will be addressed experimentally using a separate-effects approach. Ultimately, the purpose of experimental studies is to build confidence in the computational models and simulations to help ascertain the feasibility of the DPC filling process.

A separate-effects approach helps to discern the impact of complex phenomena that ultimately affect injectability and void filling due to mechanical interactions between the molten liquid and various interior surfaces of DPCs. While computational fluid dynamics (CFD) models are capable of resolving the physics of fluids, they do not include the complex physical interactions between fluids and surfaces or the intricate geometric details of DPC interiors. Typically, meso-scale effects such as surface wettability (i.e., contact angle between the fluid and the surface) and surface tension of fluids are modeled in a parametric form that defines a simple *viscous shear*. However, the stochastic variability of surfaces (such as surface roughness), and the effects of joining and intersections may have drastic impacts on the interaction between fluids and surfaces. In a physical configuration in which fluid flow is determined by a significant pressure differential, these surface effects may not be dominant. However, for this physical configuration and the planned filling process, the importance of a thorough understanding of interactions and the validation of computational models cannot be understated. Moreover, the physics of gas entrapment and void formation is not well understood.

As single-physics computational models are validated and confidence is built, a multiphysics simulation framework that couples fluid flow, thermodynamics of fluids, and heat transfer phenomena will be investigated. The multiphysics computational models and simulations will then be validated through experiments that properly address these phenomena. These models will be critical in narrowing down the choices of candidate filling materials. This capability will also be instrumental in determining whether an external heating source will be needed, and if so, whether it will be used to design such a system. The multiphysics simulation capability may require expansion to include structural analysis. The impact of radiation hardening on mechanical properties may require additional experimental studies. Finally, identification and/or development of process instruments may be required to certify the filling process with a reasonable confidence level.

The following section presents the experimental system setup designed and built in support of the initial computational models and simulations of filling a DPC through its drain pipe. The initial experimental setup is intended to provide high-level integral data such as filling time and entrapped void fraction (determined through narrow-range level monitoring) to allow for verification and/or calibration of viscous shear parameters.

3.1 Description of the Experimental Setup

To simplify the computational models to reduce runtime and avoid numerical instabilities, spacer grids are simplified by removing detailed mechanical features. These features are fully represented in the experimental setups to guarantee that their characteristic effects are captured experimentally.

The ORNL team has decided to demonstrate the filling process in two experimental setups for initial testing. The first experimental setup mimics the computational model—with the exception of detailed mechanical features in spacer grids as stated earlier—and is intended to provide supporting data for injectability of various fluids through the drain pipe, identification of a sustainable filling rate, and resulting filling time and entrapped void space. The first setup will primarily be used for experimental demonstration of the filling process with various fluids used in the CFD simulations, as shown in Table 1.

The second experimental setup is intended to provide insight into the formation of voids in intricate geometries, such as the small and irregular spaces between the fuel rods and the springs and dimples in spacer grids. The primary focus of this setup is to provide a flexible experimentation capability while being as close to the real geometric configuration as possible. A salient feature of the second experimental setup is its modular construction and its easy disassembly. This setup will use a surrogate filler material with a low melting point, such as the paraffin wax, which melts at 64°C. This will allow for visual inspection of the filled volume, particularly to understand coalescence of multiple smaller void formations into larger voids.

3.1.1 Experimental Setup Assembly Parts

The DPC filling tests currently use scaled down models to minimize material cost and expedite the testing process while maintaining a high level of feature integrity with the actual canister design. The initial phase of testing will involve the use of liquid (water / glycerin) media to test the experimental apparatus and setup controls and to establish empirical data benchmarks for fluid dynamics simulations. The ORNL team procured three types of spacer grids from Westinghouse: (1) a 17 × 17 standard structural grid, (2) a protective (P)-grid, and (3) an intermediate flow mixer (IFM) grid. While these spacer grids are available to the team, some custom spacer grids are also being fabricated through a subcontractor to closely match the specifications [14]. The custom fabricated spacer grids will be used in the initial experiments, while the Westinghouse spacer grids will be used in later phases of the demonstration work [15].

A second experimental apparatus will also be fabricated to facilitate the use of paraffin as the filler material that can undergo phase change at a low solidification temperature. This apparatus will deviate only slightly from the liquid apparatus and will allow components of high interest to be removed and disassembled to analyze the filled space. The spacer grids for this experimental setup will be custom fabricated in a manner to allow for disassembly for post-experiment visual inspection.

The designs for each of these apparatuses are detailed below.

3.1.1.1 Liquid-Only Apparatus

The liquid-only design, as shown in Figure 21, uses polycarbonate and acrylic parts for the majority of the housing components to facilitate observations of the filling process. The canister is made from 10-inch outer diameter (OD) × ¼-inch thick acrylic tubing, and the outer basket is made from machined sheets of polycarbonate which are assembled with slot features and small fasteners. The upper and lower flanges are also made from ½-inch thick polycarbonate sheets. Two split ring flanges and 16 flanged socket head cap screws mate with a groove cut into each end of the outer container's face, compressing a gasket at each end to effectively seal the ends and prevent leakage of the liquids. A ball valve is installed near the bottom of the container to aid in draining the apparatus at the end of the experiment. The internal components are modeled as closely to the true dimensions (scaled) as possible.

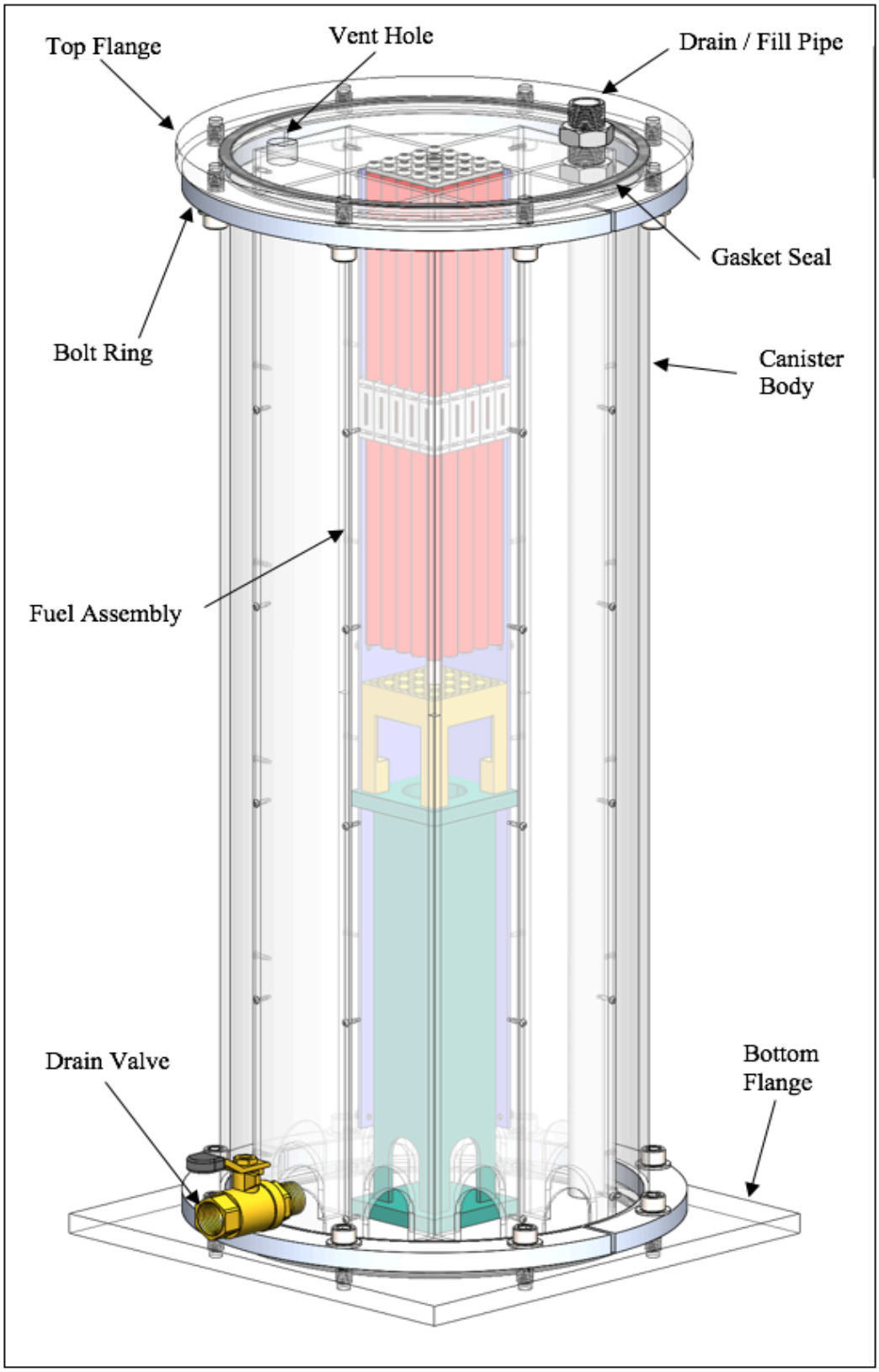

Figure 21. Polycarbonate Canister with Five-Cell Basket for Liquid Experiment.

The basket structure is the left image in Figure 22, and the bottom spacer (green), bottom nozzle (yellow), the fuel assembly (red), and the spacer grid (white), neutron absorber (gray), and the guide tube (pink) are shown as the right image in Figure 22. Figure 23 presents an artist rendering of the experimental setup.

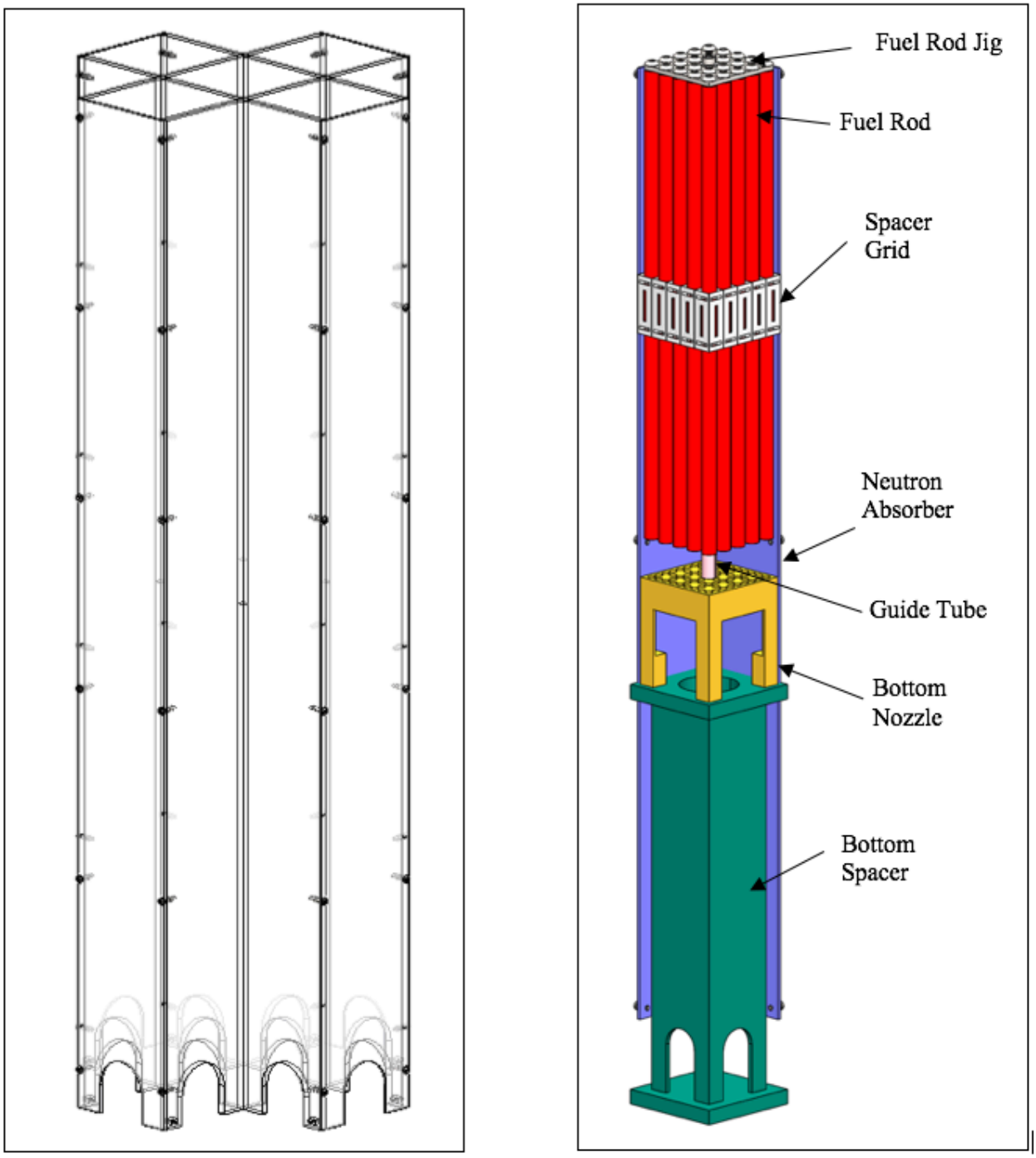

Figure 22. Polycarbonate Outer Basket (Left), and a Stack of the Fuel Assembly (Right).

Figure 23. Artist's Rendering of the Experimental Setup.

As mentioned above, ORNL received three types of spacer grids from Westinghouse. To use these grids in the experimental setup, multiple 5 × 5 grids can be created by carefully cutting the original parts. Alternatively, the original Westinghouse spacer grids can be preserved to be used in an experimental setup that uses a full-scale assembly (e.g., 17 × 17) in the later phases of the project.

Bardet et al. [14] custom fabricated a series of scaled spacer grids that closely match the original grid specifications. An example 5 × 5 spacer grid design is shown in Figure 24 and Figure 25. ORNL is collaborating with this team for fabrication of custom-made spacer grids.

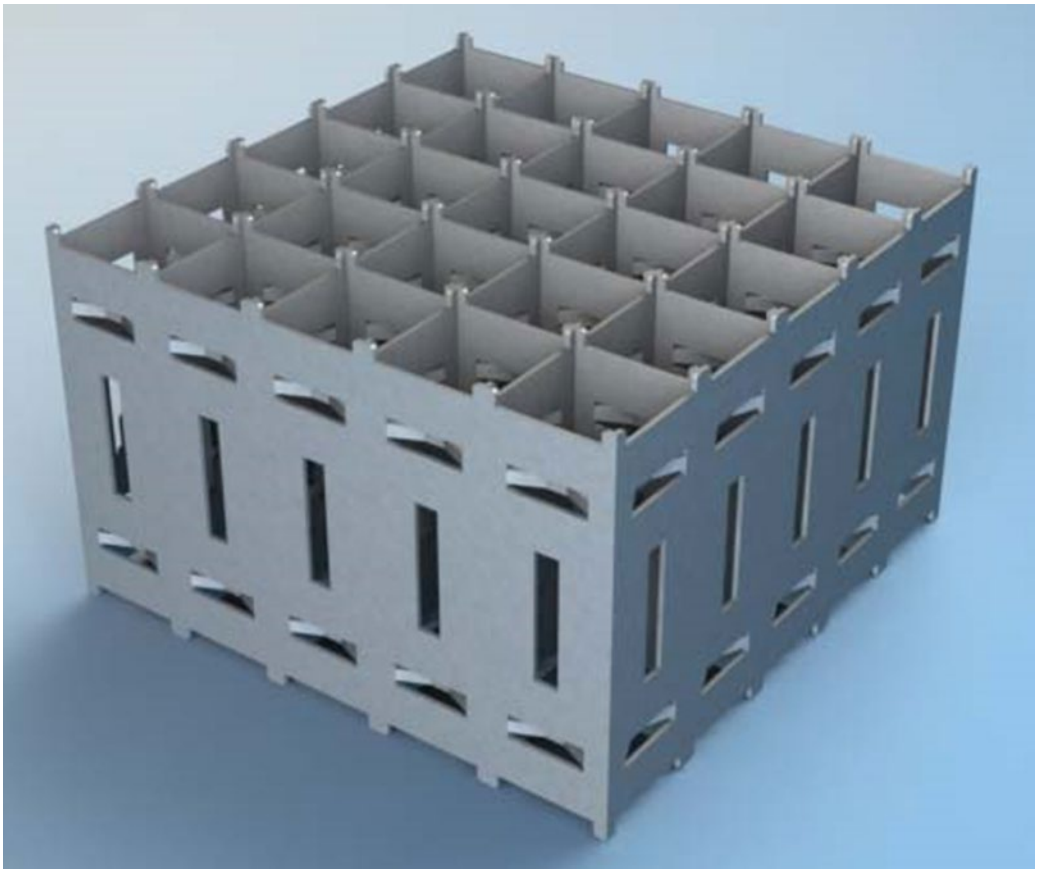

Figure 24. Side View of Spacer Grid (5 × 5) without Mixing Vanes [10].

3.1.1.2 Paraffin Filling Experiment

This design also uses polycarbonate and acrylic parts for the majority of the housing components to facilitate observation of the filling process. The container is made from 10-inch OD × ¼-inch thickness acrylic tubing which has been split into two identical halves, as shown in Figure 26. These halves are assembled using two split ring flanges and 16 flanged socket head cap screws that mate with a groove cut into each end of the outer container face. Two or more hose clamps are also used around the outer circumference to secure the canister. The edges are sealed with compressed rubber gaskets, which can be accompanied by room temperature vulcanizing (RTV) sealant if necessary. Gaskets are also located at each end of the container and are compressed by the split ring flanges. The outer basket is made from machined sheets of polycarbonate that are assembled with slot features and small fasteners. The upper and lower flanges are also made from ½-inch thick polycarbonate sheets.

The internal components are modeled as closely to the true scaled dimensions as possible, but to facilitate the disassembly of components once the paraffin has solidified, certain components have been modified.

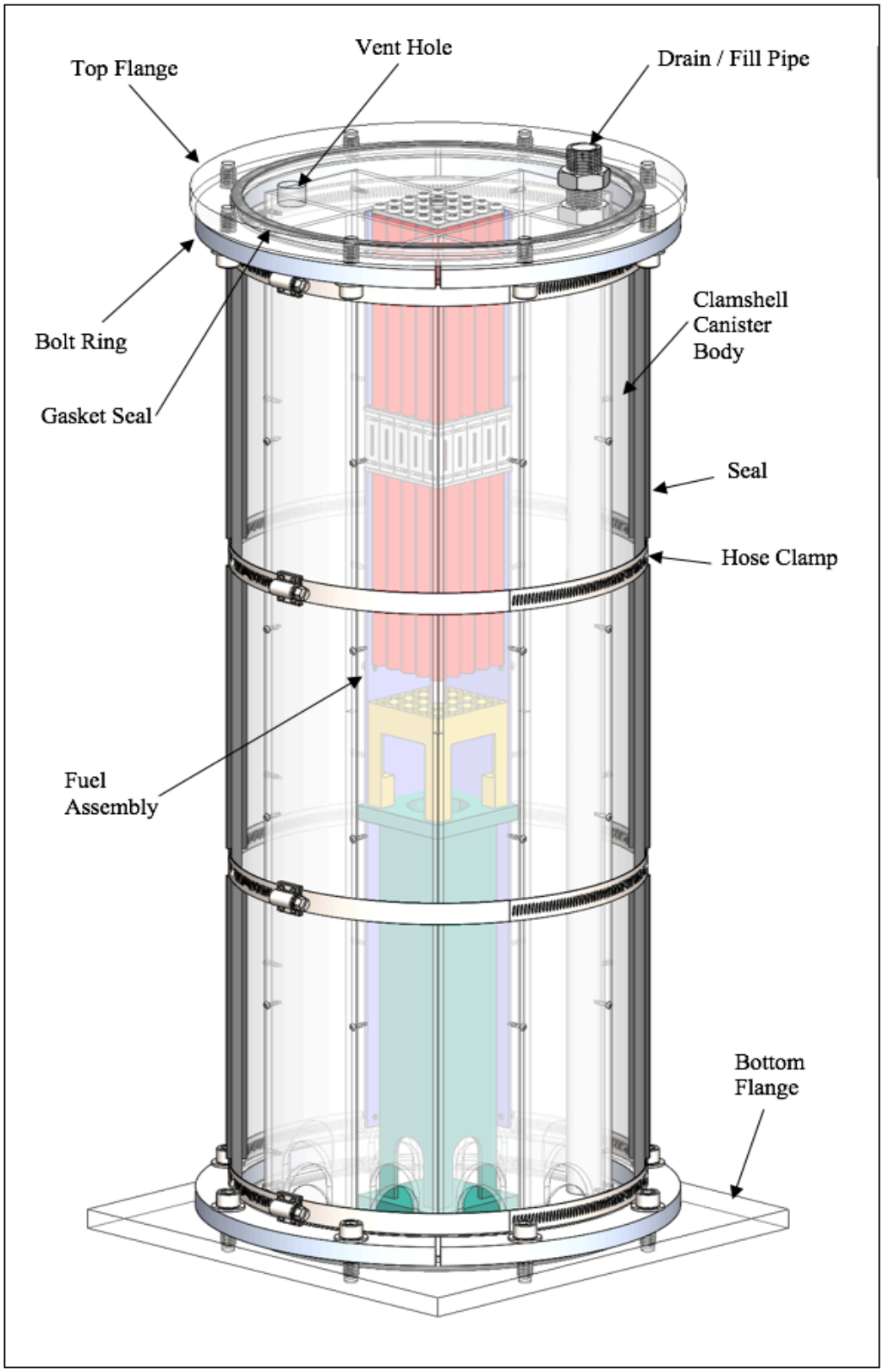

Figure 25. Polycarbonate Canister with Five-Cell Basket for Paraffin Experiment.

The grid spacer design has been modified to be easily disassembled by using upper and lower plates which contain slots to capture the grid panels. The grid panels are also modified to have tabs at each end to mate with the upper and lower plates. Figure 16 shows details of the grid panels. Figure 27 shows the exploded view of the customized modular grid assembly. The fully assembled custom grid is show in Figure 28.

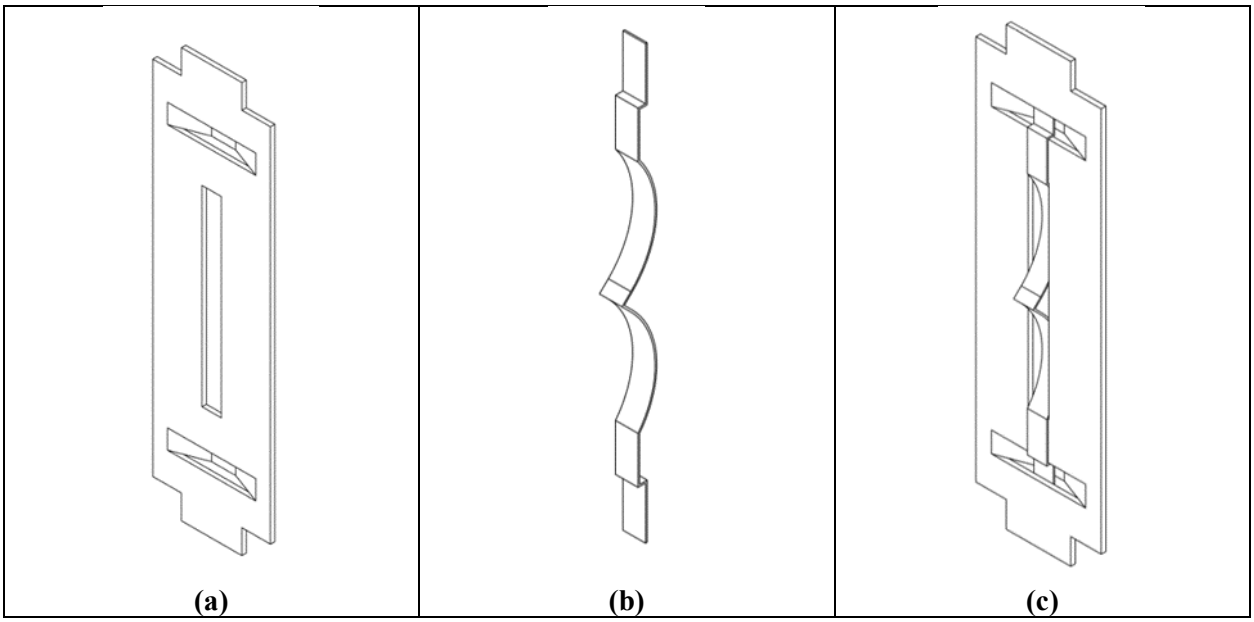

Figure 26. (a) Custom Spacer Grid with Dimple, (b) Custom Spacer Grid Compressed Spring, and (c) Custom Spacer Grid Panel with Dimple Weldment.

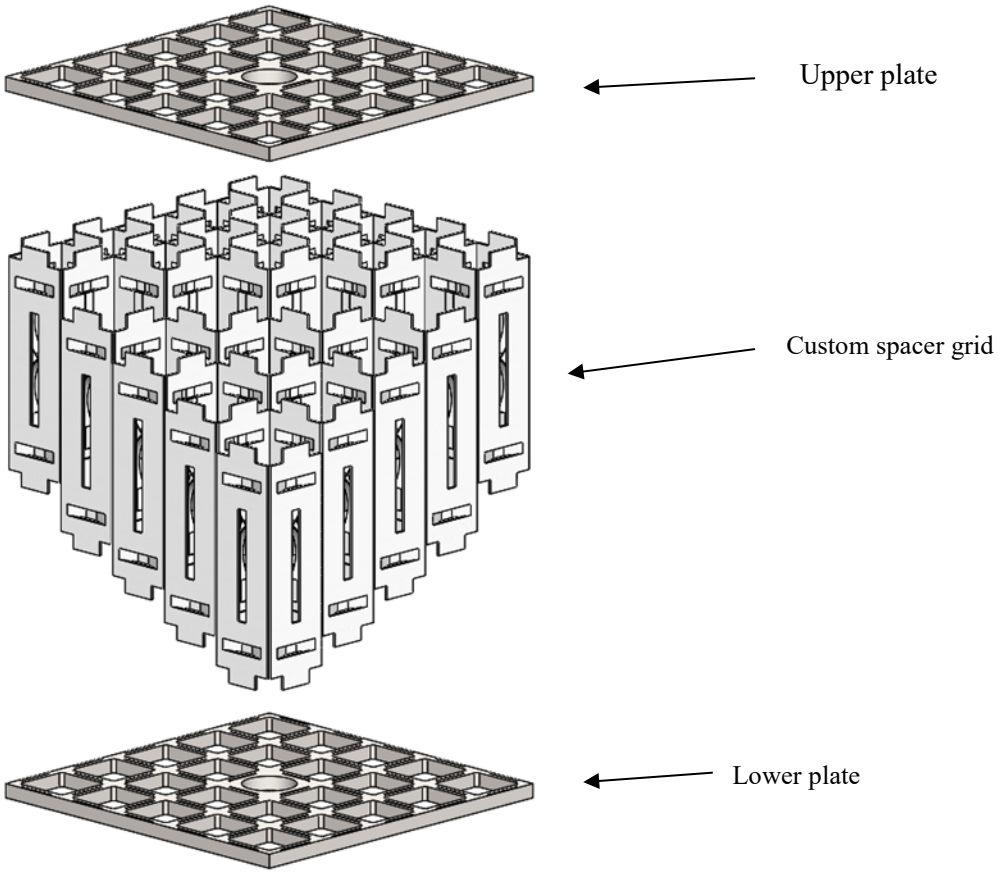

Figure 27. Exploded View of the Custom Spacer Grid Assembly.

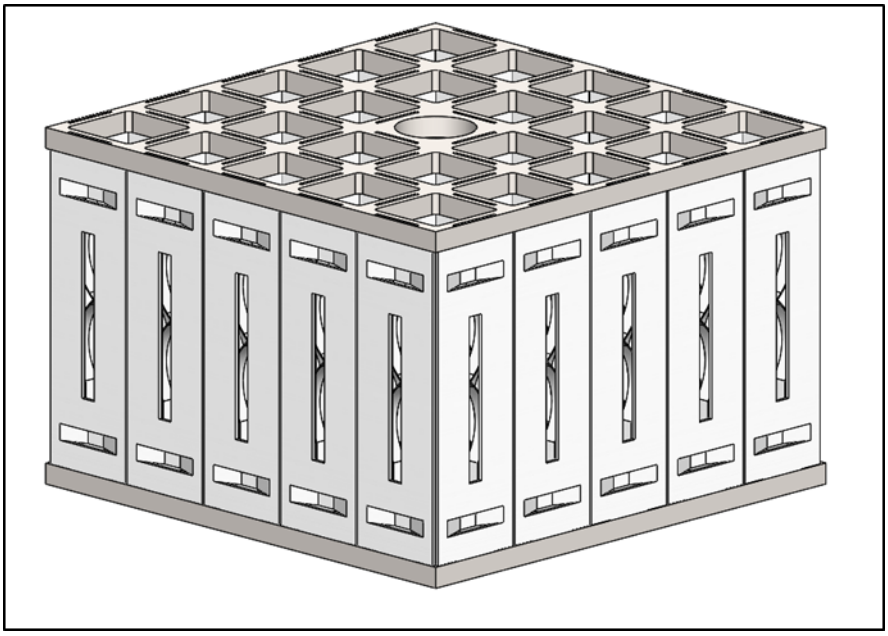

Figure 28. Fully Assembled Custom Modular Grid.

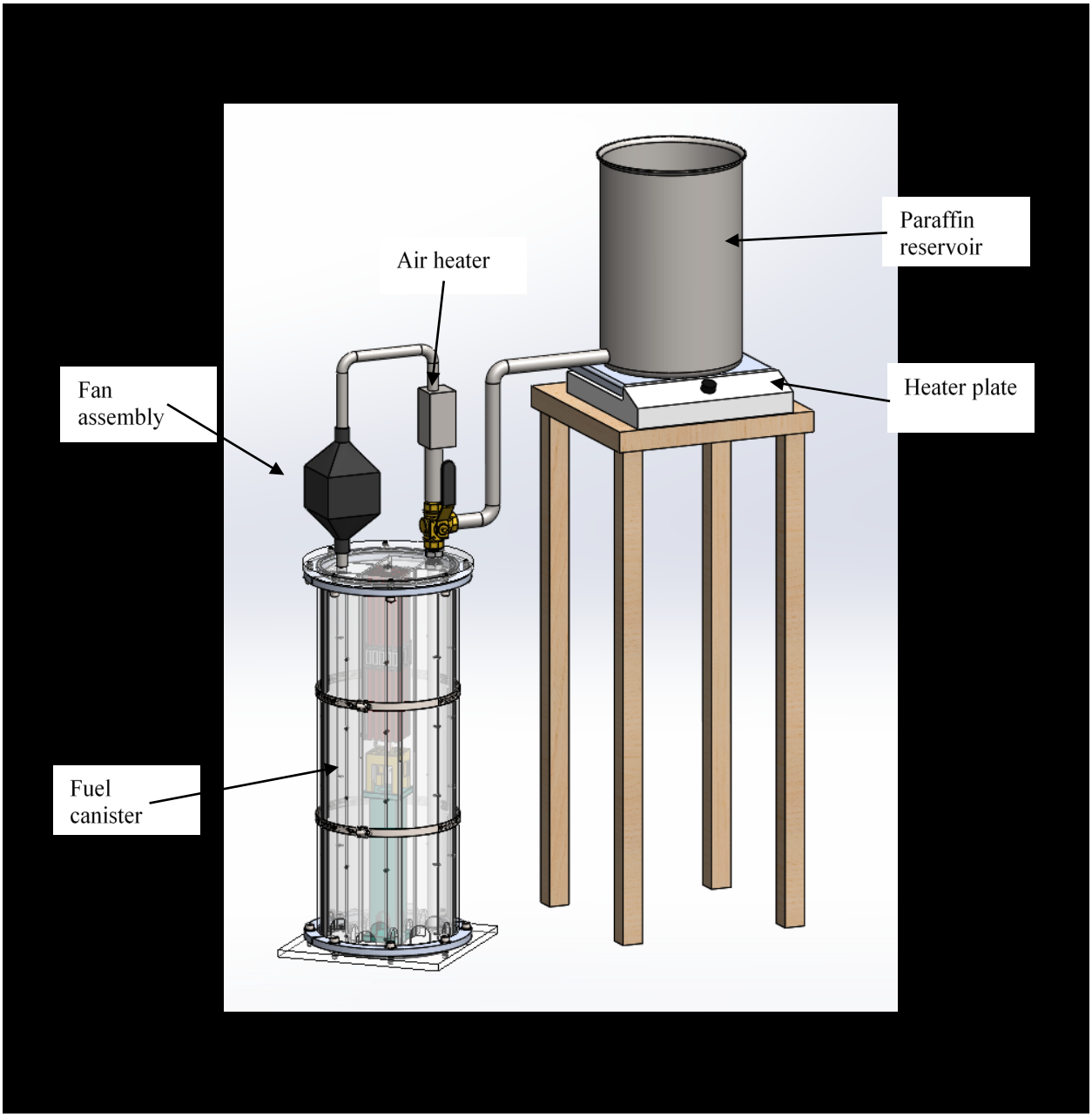

Figure 29. Set-Up for the Paraffin Experiment.

The experimental set-up shown in Figure 29 consists of a split canister assembly, an air heater, a paraffin reservoir, and a three-way valve. Initially, the three-way valve will be positioned towards the air heater tubing. The inline air heater will heat the air being circulated through the heater by the fan connected to the vent hole of the canister. A thermocouple inside the canister will register the air temperature. Once the temperature inside the canister has reached 60°C, it will be ready to be filled with paraffin. A small relief valve will also be installed on top of the upper flange to allow the air to escape as it is being displaced by the paraffin filling the canister.

Turning the three-way valve towards the paraffin reservoir will cause the paraffin to start flowing into the canister. Another valve next to the paraffin reservoir (not shown) will be used to control the paraffin flow rate. To ensure that the paraffin does not solidify before it has completely filled the canister, heat tape will be wrapped around the canister, piping, and valves. The temperature setting on the heat tape will ensure that the paraffin is maintained at 60°C. Multiple thermocouple readings will be used to ensure uniform heating during the filling experiment. Power to the heat tape, heating plate, and the air heater will have logic to ensure that components are not overheated while also ensuring that adequate temperature of the air and paraffin are maintained.

3.1.2 Experimental Setup Assembly Parts Acquisition Status

All drawings (Table 3) were finalized and forwarded to machine shops for fabrication. ORNL team is expecting to order all other parts for conducting the experiment by the end of August, 2018. Table 4 presents the parts acquisition status as of 31 August, 2018.

Table 3. Drawing part number and quantities being fabricated.

DWG	ITEM	Quantity
284-DPC-1110 (Assembly)	Panel weldment (with dimple)	25
284-DPC-1111 (Part)	Panel with dimple	37
284-DPC-1112 (Part)	Spring	37
284-DPC-1120 (Assembly)	Panel weldment (without dimple)	12
284-DPC-1121 (Part)	Panel without dimple	12

Table 4.Parts list.

Item	Specification	Cost	Vendor Info
Fan	1053-1116-ND	$100	Digikey
Heater	AHPF-061	$345	Omega Engineering (not used)
Plate heater (for paraffin wax)	0-300°C, hot plate	$115	3118K52, McMaster Carr
Paraffin wax*	Nature Wax C-1	$118	General Wax and Candles
SS-container with temperature gauge and shut-off valve	½-inch NPT Connection	$218.90	10 Gal BrewBuilt Kettle
Metal braided hoses	½-inch ID (up to 350°F)	$315	McMaster Carr
3-way ON/OFF valve	½-inch ID	$100	McMaster Carr
High precision flow valve	¼-inch tube	$380	McMaster Carr
Flexible heating tape	½-inch wide	$1,500	BriskHeat
Thermocouple and reader	--	--	Already have them

3.2 Planned Measurements and Instrumentations Used During and After Filling

The key quantities of interest for this initial experimental work are the following:

- Flow rate of the filler material,
- Filling time, and
- Volume of entrapped gas.

The flow rate of the filler material can be measured with a high-sensitivity low-flow meter or a micro-flow meter. The filling time will be measured by a chronometer triggered by the control gate of the filler material flow controller. The volume of entrapped gas will be calculated by the level of the liquid using a narrow-range level sensor.

In the paraffin filling experimental setup, the guide tube, fuel rods, and the spacer grids will be coated with mold release for easy removal of the interior pieces in contact with paraffin. Once the apparatus is filled with liquid paraffin at temperature, the system will be allowed to cool down to its solidus temperature. After sufficient time for temperature equilibrium, the canister clam shells will be opened to expose the solid paraffin—with potential trapped gas volume. The paraffin wax will be sliced to allow access into the interior regions. Once the inner fuel assembly is accessed, the guide tube will be removed first, followed by the upper and lower plates of the spacer grid assembly. Working from the outer regions, individual spacer grid plates will be removed to expose the paraffin. The fuel rod corresponding to the area will then be pulled straight out. Sections of these regions can then be sliced using a thin knife to obtain cross sections of the paraffin to evaluate gas entrapment (void spaces). This procedure will then be repeated for all regions of the fuel assembly.

3.3 Discussion

Two initial experimental setups were designed for liquid and paraffin experiments. Data collected from these experiments will be used to validate the filling simulation described in Section 2. The paraffin experiments will require external heating like any molten metal–based fillers and will provide valuable experience to inform a full-fledged experiment using molten metal fillers. All the drawings for various initial experiment setup parts have been completed, and procurement of the parts has been initiated. ORNL has also received three spacer grids from Westinghouse. The ORNL team expects to complete the initial setup by end of FY 2018.

4. CONCLUSION

A multi-phase approach as described in the joint workplan [4] culminating to a full-scale demonstration and a fully validated multiphysics simulation/prediction capability are being pursued to support direct disposal of DPCs. An acceptable filler should establish the probability of criticality in DPCs during the disposal time frame to be below the probability threshold for inclusion in a repository performance assessment. As discussed in the introduction, the filler option to support direct disposal of DPCs is being investigated in parallel with the other options such as criticality consequence assessment. This report describes the initial single physics CFD model developed to simulate the filling process and the planned experimental setups to validate the CFD simulation. The initial filling simulations of the lower region (mouse holes) of a prototypic DPC show successful removal of the inner space voids and smooth (even) liquid level progression. The filling through the drain pipe is currently being investigated as a decoupled process due to complexity of modeling flow in a narrow long pipe. A flow experiment through a pipe to understand any issue related to filling a DPC using drain pipe is also discussed in this report. Additionally, the initial experimental setups have been designed, and the various assembly parts are being procured.

This page is intentionally left blank.

5. REFERENCES

1. StoreFuel and Decommissioning Report, Ux Consulting Company, LLC ("UxC"), Vol. 20, No. 238, June 2018.
2. E. Hardin et al., *Investigation of Dual-Purpose Canister Direct Disposal Feasibility (FY14)*, FCRD-UFD-2014-000069 Rev.1, October 2014.
3. J. B. Clarity, K. Banerjee, H. K. Liljenfeldt, and W. J. Marshall, "As-Loaded Criticality Margin Assessment of Dual-Purpose Canisters Using UNF-ST&DARDS," *Nuclear Technology,* 199(3), 245–275 (2017).
4. *Joint Workplan on Filler Investigations for DPCs*, Sandia National Laboratory, SFWD-SFWST-2018-000481, Rev.0, December 2017.
5. Holtec International, *Final Safety Analyses Report for the HI-STORM 100 Cask System*, 2010.
6. CD-Adapco, *STAR-CCM+ 13.02 Theory Guide*, 2015.
7. https://mdx.plm.automation.siemens.com/star-ccm-plus.
8. I. Zadrazil and C. Markides, "An experimental characterization of liquid films in downwards co-current gas-liquid annular flow by particle image and tracking velocimetry," *Int. J. of Multiphase Flow* 67, 2014.
9. A. Padmanaban, *Film Thickness Measurements in Falling Annular Films*, Thesis McS, University of Saskatchewan, 2006.
10. P. Kapitza, Wave flow of thin layers of a viscous fluid, Collected papers of Kapitza, Pergamon Press, 1965.
11. S. V. Paras and A. J. Karabelas, "Properties of the liquid layer in horizontal annular flow," *Int. J. Multiphase Flow* 17 (4), 439–454 (1991).
12. L. B. Fore and A. E. Dukler, "Droplet deposition and momentum transfer in annular flow," *AIChE J.* 41 (9), 2040–2046 (1995).
13. H. M. Prasser, A. Boettger, and J. Zschau, "A new electrode-mesh tomograph for gas–liquid flows," *Flow Measure. Instrum*. 9, 111–119 (1998).
14. N. A. Weichselbaum et al., *Surrogate Spacer Grid Design for Fluid-Structure Interactions Studies in Fuel Bundles*, The George Washington University, Washington, DC.
15. A. Rubin et al., *Volume I: Experimental Database and Final Problem Specification, OECD/NRC Benchmark Based on NUPEC PWR Subchannel and Bundle Tests (PSBT)*, November 2010.

This page is intentionally left blank.

APPENDIX A

This appendix documents work performed supporting the US Department of Energy (DOE) Nuclear Energy Spent Fuel and Waste Disposition, Spent Fuel and Waste Science and Technology, under work breakdown structure element 1.08.01.03.05, "Direct Disposal of Dual Purpose Canisters." In particular, this appendix fulfills the M3 milestone, M3SF-19OR0103050115, "Initial validation of CFD filling simulation," as Revision 2 to M4SF-18OR010305017, "Unit test plan for filler demonstration," within work package SF-19OR01030501, "Direct Disposal of Dual Purpose Canisters–ORNL."

This appendix presents (1) the CFD filling simulation of the spacer grid region of the assemblies using the model described in the main body of the report, and (2) data collected in a laboratory experiment using surrogate fillers for validating the simulation results. In summary, this appendix presents the current simulation and experimental validation status of the DPC filler project. This report will be revised periodically to document step-by-step development of a fully validated multiphysics tool that can be used for simulating the DPC filling process using various filler materials. This multiphysics tool is also envisioned to be used to select a small set of filler materials for further laboratory testing (e.g., corrosion properties, radiation damage).

A-1. Simulation Progress

A-1.1 Bottom Nozzle Filling Simulation

The main body of this report primarily presents the CFD filling simulation of the mouse hole region and the progress made to simulate the lower grid region. Since the time of report release, the following progress is made: the lower grid simulations were finalized, and the spacer grid region was fully simulated. The results are briefly presented below. This completes the initial scope of filling simulations for model validation. The simulations will continue with modeling of real canister systems for numerical filling evaluation.

The lower assembly grid region occupies the area of the lower tie grid and the upper section of the assembly stand. A part of the geometry is skipped (shortened) to save computing time by transposing the lower tie grid to fit over the mouse holes region. The rationale assumes that the flow topology (level velocity and liquid fraction) at the entrance of the lower grid is the same as the flow topology at the exit of mouse holes. Technically, this simulation is accomplished by mapping data between nonconformal domains.

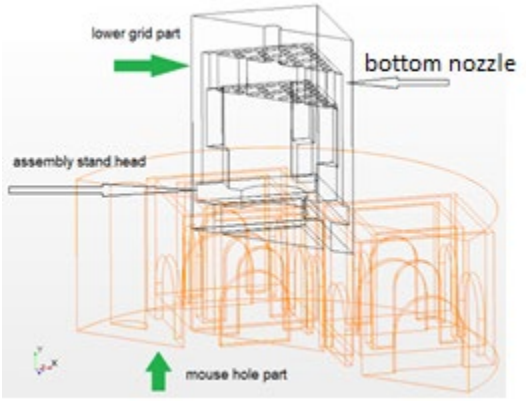

Figure A-1. Lower Tie Grid Position Relative to Mouse Holes Region with All Important Features Indicated.

The components and their relative positioning are shown in Figure A-1. The mouse hole region is shown in orange to distinguish the components. The lower grid section has an overall height of 113 mm and is set to overlap the mouse hole region, with 15 mm to allow for data mapping. The lower grid section is meshed with about 100,000 elements. The large number of elements is due to the holes in the lower assembly grid.

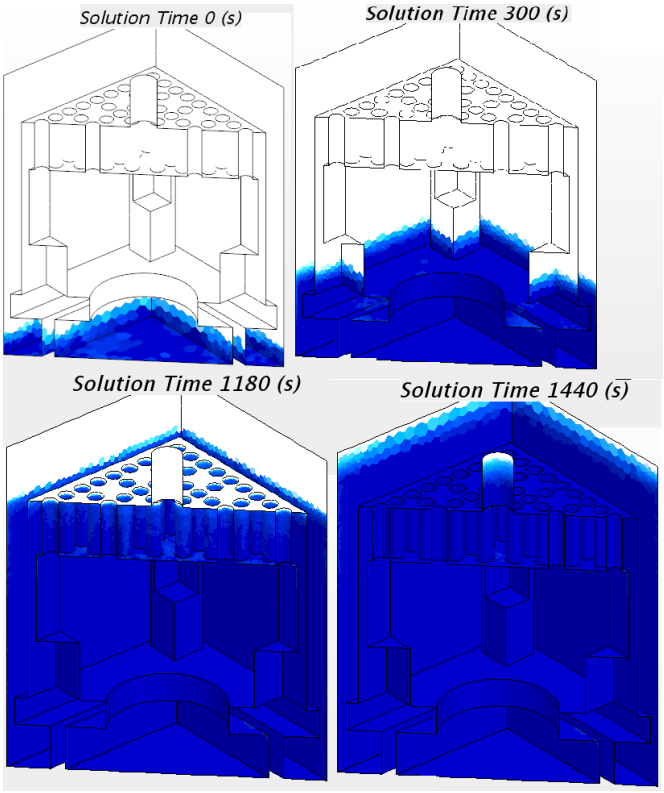

Figure A-2. Filling Simulation of the Lower Assembly Bottom Nozzle Showing Four Instances of the Filling Process. Geometry is Clearly Visible. Liquid Volume is Blue and Shows a Smooth and Continuous Level Progression.

The runs for water, glycerin and silicon oil were successfully performed and showed no trapped voids. They were executed on 96 cores (three nodes × 32 cores each). The total computed physical time was 1,440 s. The level progressed smoothly, as in the previous DPC section (mouse holes), without any anomalies. Four snapshots of the entire lower grid section showing the level advancement are plotted in Figure A-2.

Because the lower grid region simulates only one part of one fuel assembly, to properly set up the inlet flow, the filling rate is recalculated based on the total volume of this region and the volume of the entire canister mock up section with the same height. This results in an equivalent filling rate of 0.138 cc/s.

To allow for axial tracking of the filing process and identification of eventual voids, several cross sections of the domain were plotted as shown in Figure A-3. The cross sections are taken in the symmetry plane (mid-section) and at the 45-, 90-, and 135-degree sections. The information from these plots demonstrates even level progression and in all parts of the region. The most critical area for void formation is the tie grid, but the solution shows successful filling.

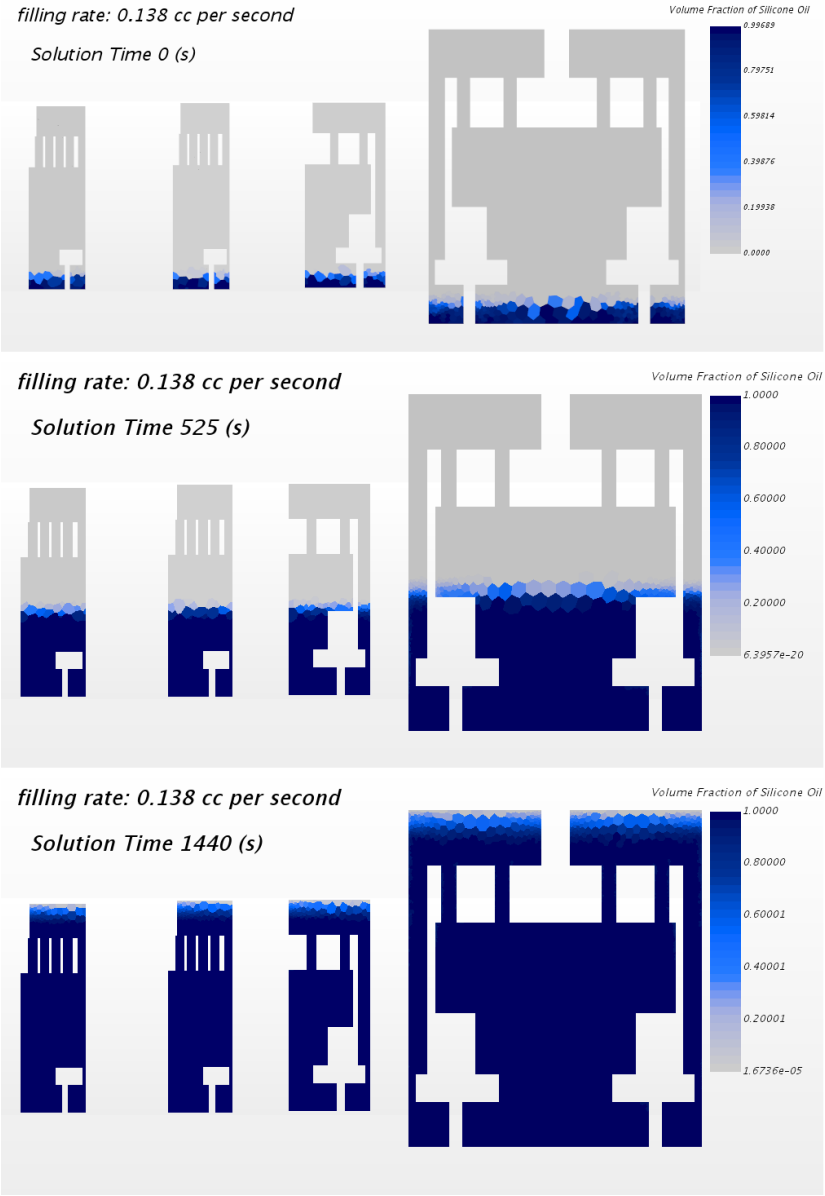

Figure A-3. Domain Sections Tracking the Level in the Lower Grid Region. Three Instances of Time Are Plotted at the Beginning, Near the Middle, and at the End of the Process.

A-1.2 Spacer Grid Filling Simulation

The spacer grid region of the domain includes the first rod spacer grid with some of its features (vanes) simplified. Since all grids are the same for the test assembly being modelled, simulating only one is acceptable to prove the filling of voids. In this case, no domain transposition was applied, and the data mapping is continuous from the bottom nozzle region. Instead of removing a section between the two regions, part of the domain occupied with rods is shortened to save computing time. In the real geometry, the spacer is located further up in the rod bundle, but in the simulation, the spacer was translated down almost immediately after the rods start.

Another change is made in the simulation to save compute time. The filling rate is increased five times, from 0.138 to 0.69 cc/s. This was done because if the filling is successful at a higher rate, it should be successful at any lower rate.

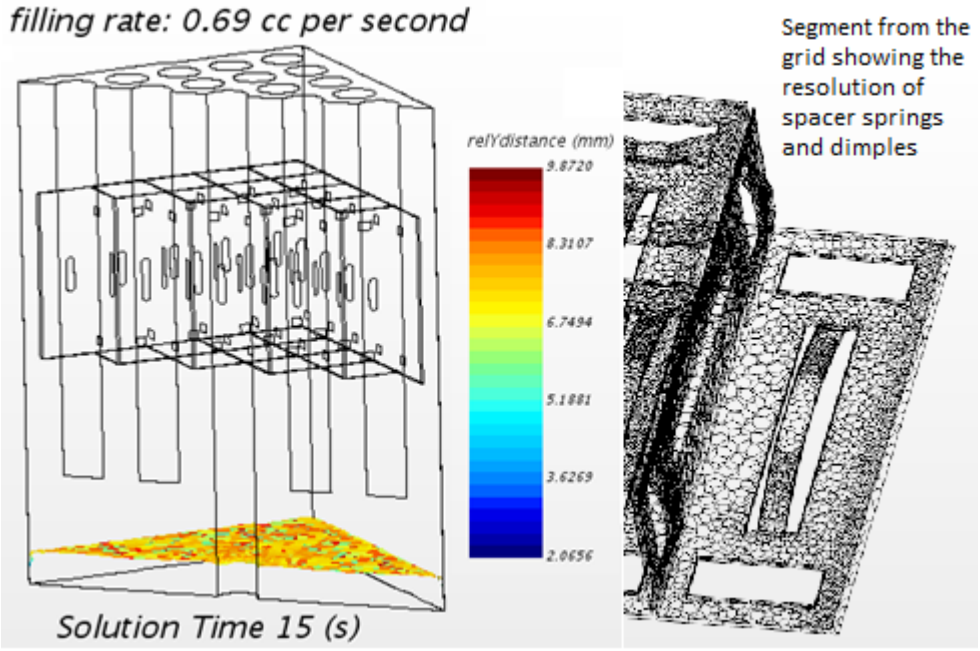

Figure A-4. Spacer Grid Region, Including Rods. The Outline Shows the Location of the Spacer Grid and Level 15 s after Filling Started. The Level Is Measured from the Floor of This Region.

The spacer grid region is shown in Figure A-4 along with a newly implemented function to compute the liquid level relative to the region floor. The function captured the level unevenness by giving the distance to the floor of any fluid elements that have more than 70% liquid content. The scale shows that the computed level varies between around 6 and 10 mm for the plotted time instance. This indicates a 4 mm level accuracy, mainly due to the resolution of domain discretization.

The overall filling of the region is shown in Figure A-5. As in all previously discussed regions, the liquid front progressed without any anomaly. The first graph on the left in Figure A-5 shows the initial state after the level has been mapped from the lower grid region. The middle graph displays the filling at the location of rods, and the graph on the right shows the filling in the spacer grid.

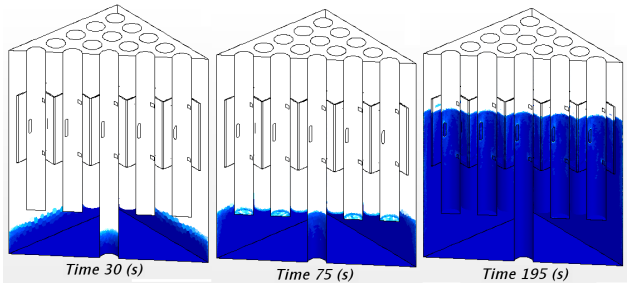

Figure A-5. Filling of Spacer Grid Region. Three Instances of the Process Are Shown: the Beginning after Mapping, at the Position of Rods, and at the Spacer.

Work continues with implementation of more controls that would allow for evaluation of the uncertainty in level determination. The concept of level tracking is being used to determine if any voids have formed, and it provides a quantitative measure of the detectable void size.

A-2. Filling Demonstration Progress

The objective of the initial filing demonstrations was to gain confidence in the computational simulations. ORNL developed a prototypical DPC mockup to investigate the injectability of liquids through the drain pipe and to provide insight for the filing operation by collecting validation data for the initial CFD simulations. Once the computational models are validated, they can be used to narrow down the candidate fillers to eliminate excessive testing and demonstration.

A-2.1 Experimental System and Configuration

The ORNL team designed and built two experimental setups to be used for the initial demonstrations. The first setup, a liquid-test apparatus, is being used to practice using fillers with different densities and viscosities and to collect validation data for the simulations. This apparatus was designed to employ nonhazardous liquids. The second experimental setup is intended to provide insight into the formation of voids in intricate geometries, such as the small and irregular spaces between the fuel rods and the springs and dimples in spacer grids. This setup will use a filler material with a low melting point, such as the paraffin wax, which melts at 64°C. This will allow for visual inspection of the filled volume, particularly to understand coalescence of multiple smaller void formations into larger voids.

The liquid-test apparatus is a mockup of the DPC [1], and it includes most of its real features. The DPC-filling apparatuses are scaled down models to expedite testing and minimize cost. The system is composed of an outer housing tube, an inner basket, a drain tube, support stands, lower assembly stands, assembly spacer grids, and fuel rods representing a portion of MPC32 DPC. The outer canister material is made out of acrylic to enable visual observation of the filling process. The outer housing is a 1.27 cm thick wall tube with a 25.4 cm outer diameter. The overall height is 70 cm. The canister is enclosed with a polycarbonate 1.27 cm thick bottom and top flanges. Flanges have three plugged holes at the bottom to allow for draining after testing.

The inner basket is designed to accommodate a 5 × 5 fuel bundle. The initial demonstration focuses on validation of the computational models for the lower 70 mm of the system, where the region of interest is the arched openings at the bottom of the basket. This region is referred to as the *mouse holes* in earlier simulation work. The mouse hole region is chosen to be the first test region due to its proximity to the drain tube. It is the first feature with which any type of filler will interact and through which it will propagate. The mouse hole openings were modeled at 3.81 cm wide and 3.81 cm long. The basket was fabricated from polycarbonate panels that were machined with upper and lower cut-outs to be assembled by interpenetration, as shown in Figure A-6.

Figure A-6. Basket Fabrication.

The second challenging path that any type of filler will traverse is through the inner mouse holes at the bottom of the support stands placed in the basket segments. The support bottom spacer is 27.31 cm long. The inner mouse hole openings are slightly higher at 4.45 cm long and 2.54 cm wide. These parts were fabricated from 304L stainless steel, and the lower assembly stands are welded on top. Figure A-7. shows the fabricated bottom spacers.

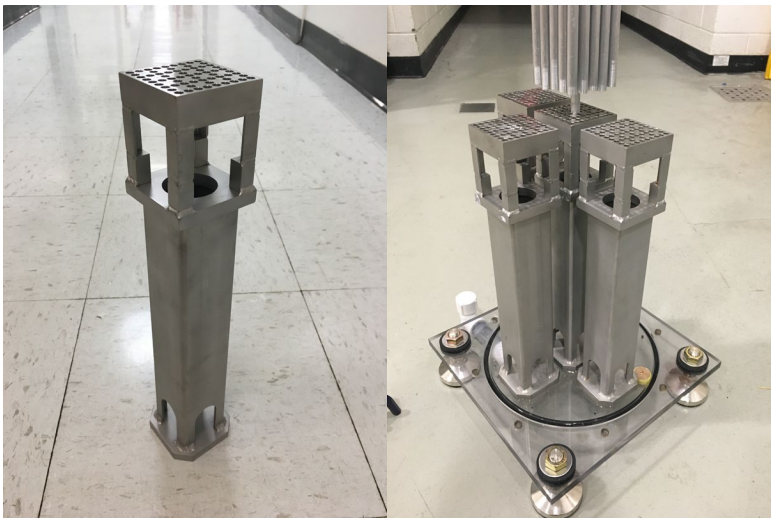

Figure A-7. Bottom Spacers.

Custom-made spacer grids (Figure A-8) were fabricated through a subcontract with Professor Philippe Bardet from George Washington University, who has experience fabricating surrogate spacer grids with realistic features. These grids allow for capturing the phenomena of interest in that region for various research topics [2]. In this case, springs and dimples are anticipated to have a profound effect during the filling process. Understanding how small spaces between the fuel rods and the spacer grid features impact bubble formation is essential for establishing a sound technical basis when down selecting filler candidates for the program.

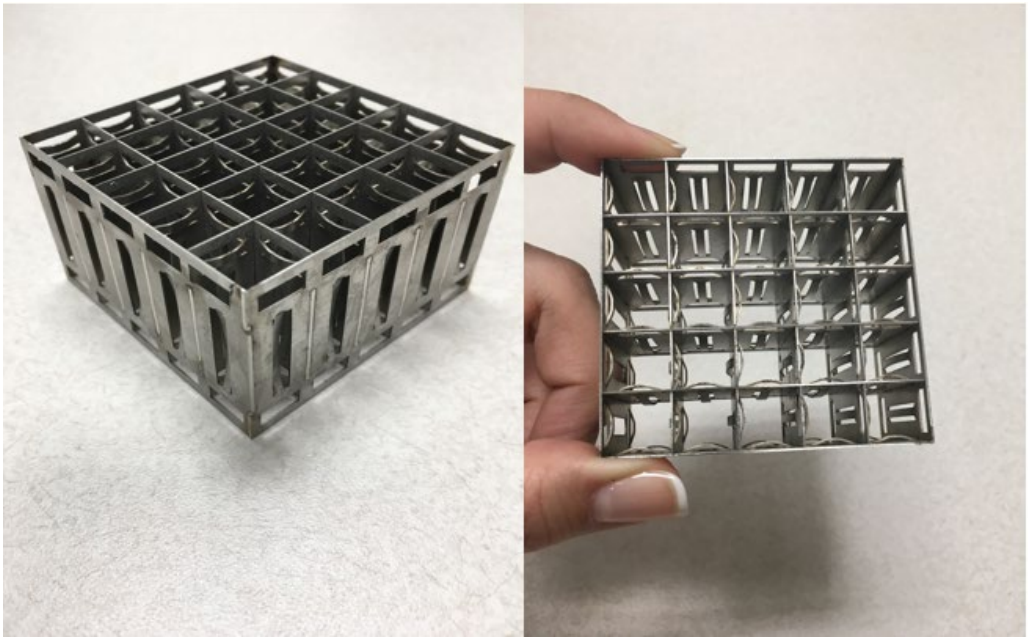

Figure A-8. Welded Spacer Grids for the Liquid Apparatus.

The complete set up is shown in Figure A-9. Measurements are taken using two level sensors inserted at different positions inside the canister. The whole canister assembly is placed on a weigh scale to collect the weigh data, and the level data is collected simultaneously by the level sensors. All output is recorded in a laptop through a data acquisition system.

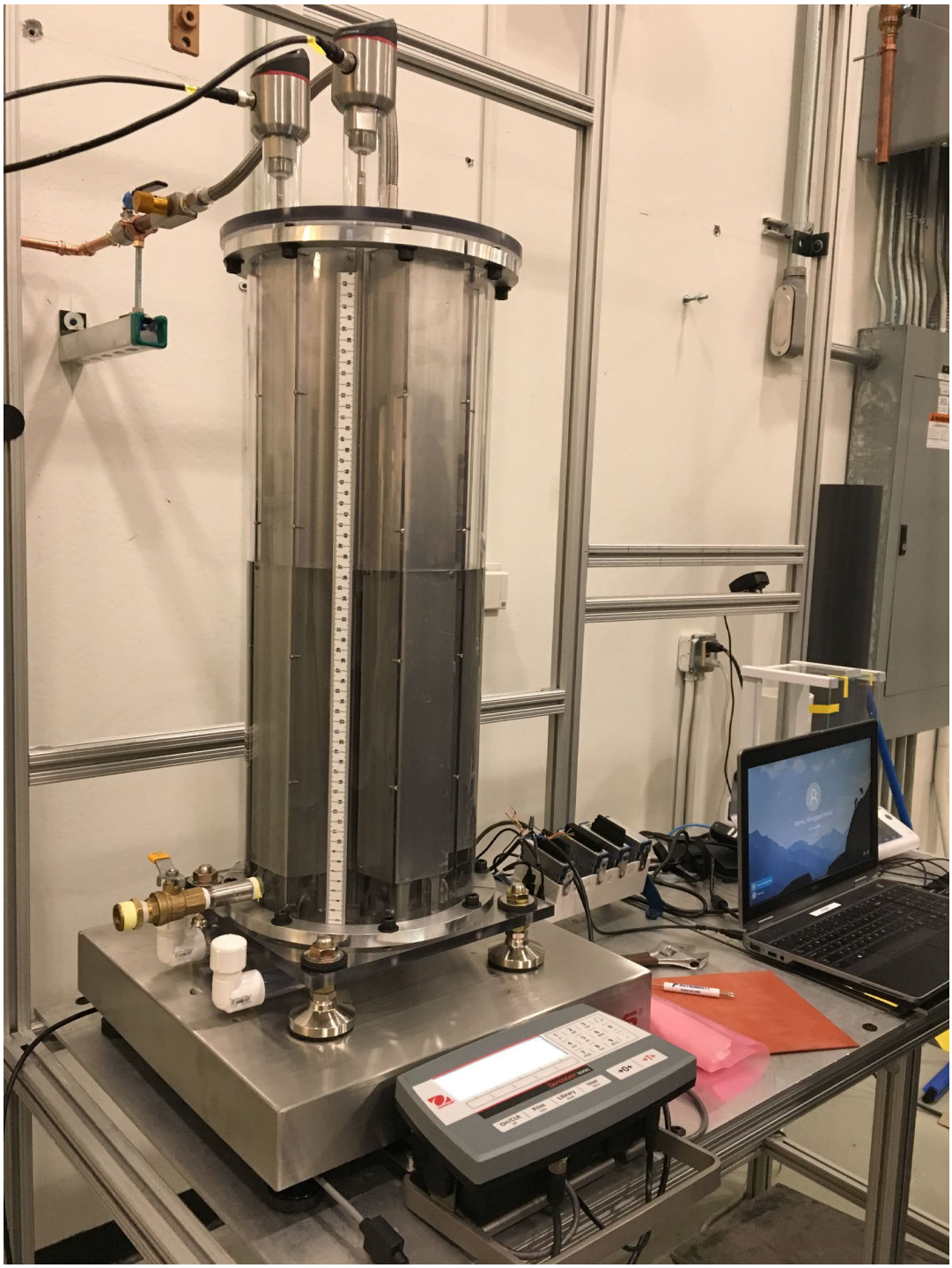

Figure A-9. Experimental Set Up for Liquid Measurements.

A-2.2 Instrumentation and Measurement Methodology

Level measurement methods were investigated to acquire real-time data during the filling process. The sensors surveyed included (1) float type level sensors, (2) conductivity-based level sensors, (3) ultrasonic level sensors, (4) capacitance-based level sensors, and (5) electrical pulse echo level sensors. Float-type sensors may present challenges, as the float takes up some space in the flow channel, thus affecting flow characteristics. Additionally, the float may potentially get stuck. The conductivity-based sensing method works on the principle of detecting changes in the conductivity of surrounding fluid and thus determining the position of the liquid-gas interface. However, this method is affected by metals in close proximity to the sensing line. This sensor type is also incompatible with nonconductive and highly viscous liquids. Ultrasonic-type level probes were also explored to assess whether they would meet the accuracy and sensitivity requirements. This method works on the principle of reflection of ultrasonic waves resulting from a sudden change of impedance along the axis of propagation—in this case the gas-liquid interface. However, since the sound waves tend to spread even with a focusing horn, the spot diameter may grow more than 70 mm at a range of 700 mm. Therefore, detection will be averaged by the ultrasonic signal reflected from other nearby objects. This method could have worked in an open tank, but this experimental set up does not meet the environmental requirements. As the spot size was found out to be larger than the free space available for detection, this sensor was eliminated from consideration. Capacitance-type level-sensing probes monitor the capacitance generated between the liquid and the tank wall. The accuracy of this sensor was found to be greater than 1.5 mm. Other sensors like radar also had similar accuracy problems (>1.5 mm), although they supported the needed range of the experiment. Finally, a reliable level sensing probe was identified that met the constraints of the experimental setup. The sensing guide pulse level sensor [3] launches a fast-electrical pulse for detecting the gas-liquid interface. This approach allows for monitoring a wide range of liquids. The transmitter generates a 4–20 mA linear output. The specifications of this sensor are summarized in Table A-1.

Table A-1. Specifications for the Guide Pulse Sensor Model FL-001

MODEL FL-001 Specifications		
Measurement range		100–2,000 mm
Resolution		1 mm
Linearity		±3 mm
Temperature characteristics		0.1 mm /°C
Undetectable area	From the top end	25 mm
	From the bottom end	10 mm
Response time to comparator output		0.4s minimum
Connection bore diameter		G3/4
Analog output		4–20 mA, maximum load resistance: 350Ω
Analog output accuracy	Resolution	1 mm
	Zero accuracy	±0.1 mA (Zero point = 4 mA)
	Full scale accuracy	±0.2 mA (Full scale = 20 mA)
Current consumption		300 mA max. (at 10V) / 120 mA max. (at 30V)
Power supply voltage		10–30 VDC

The basic detection principle of the guide pulse method is that the sensor transmits a pulse signal to the liquid along the guide probe. It then receives the pulse signal reflected off of the liquid surface and determines the distance (level) from the time between the transmission and reception of the pulse signal. The detection distance L is determined by using the formula

$$L = \frac{1}{2}\, c\, t, \tag{17}$$

where t is the time between the transmission and reception, and c is the speed of the pulse. The principle of operation is illustrated in Figure A-10.

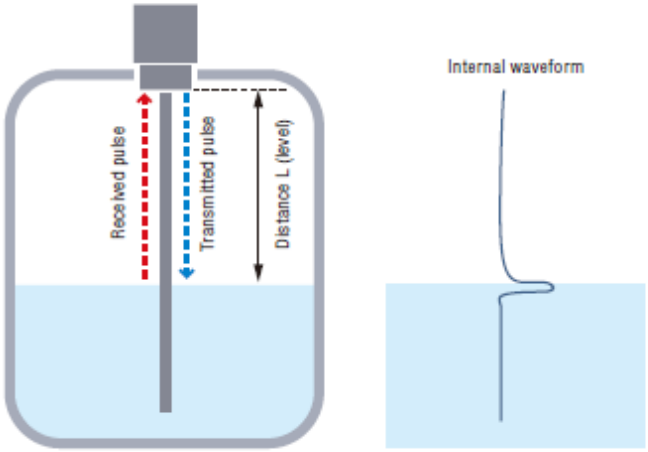

Figure A-10. Detection Principle of the Sensing Guide Pulse Method.

The model FL-001 is suitable for detecting level of water, oils, coolants, and noncorrosive liquids. It is also suitable for detecting levels of liquids containing solid particles and viscous liquids. The resolution is 1 mm, and the response time is 0.4 s.

To minimize interference, the sensor probe should be positioned away from surfaces like walls and other obstacles. Another important point is regarding the undetectable areas along the probe. The probe chosen for this experiment is 800 mm long; of that length, 25 mm from the top end and 10 mm from the bottom end are undetectable areas. To eliminate false detection and to accommodate the difference, two plastic tubes were added into the holes at the bottom flange as shown in Figure A-11. The probes are placed into those holes (centered and not touching), and the offset is considered during calibration to obtain a zero level at the bottom of the canister.

Identical units were used in two different locations for measurement redundancy.

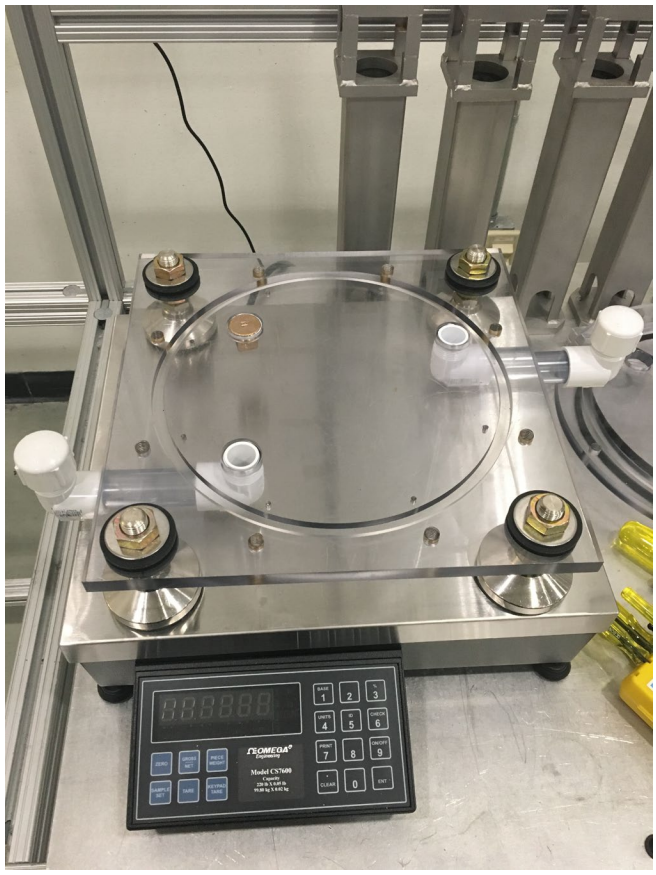

Figure A-11. Bottom Flange Modified to Accommodate the Bottom Offset of the Probe's Undetectability.

The weight of the experimental set up was measured during the filling process. This was is accomplished by placing the system on top of a digital scale and continuously monitoring the assembly's change of weight during the filling process. This method allows for verifying the flow rate, and it also provides an alternative way to infer the liquid level.

The OHAUS D52P125RQL5 Defender 5000 Low-Profile Bench Scale was chosen. This model includes a digital output port that enables real-time data acquisition. The scale's maximum capacity is 125kg ±5g

National Instruments (NI) cDAQ 9178 was used as the data acquisition (DAQ) system. Both the weight and the level measurements were converted to a 4–20 mA current signal to minimize the effect of cable lengths. A linear scaling was used to convert the current signals to weight and level readings.

The graphical user interface (GUI) used a 500 ms cycle time to acquire the data. The time stamp of the computer was used to acquire the absolute time during data acquisition. This resulted in a very accurate record of the weight measurement and level reading as a function of time.

The FL-001 pulse level sensor was observed to have stability issues in the lower levels. These issues were thought to have resulted from the metal rings that were used to clamp the canisters to the bottom flange.

Finally, the level was observed visually. A tape measure was attached to the outside of the polycarbonate canister, and a small flash light was placed underneath the canister to help illuminate the rising water level. The filling process was recorded with a camera with its own internal timer. The data were then generated by visually reading the rise of the level over the elapsed time at every 1 mm rise in fluid level.

A-3. Experiments and Results Discussion

A-3.1 Water Experiment

A bypass pipeline was installed on the main water supply to provide the water for initial calibration and testing of the experiment system. A backflow preventer, a pressure regulator, a ball valve, and a flow control metering valve were installed. A flexible hose was attached at the end to allow for easy connection to the treaded drain pipe extension.

A-3.1.1 Experimental Procedure

As described in Section 2.1, CFD simulations adopted a flow rate of 1.26 cc/sec for a half-symmetry geometry. The same filling rate was used for the liquid apparatus, but it was later found that this rate was too low for the geometry. More viscous liquids may create even more problems and may promote generation of bubbles due to surface tension forces between the wall of the pipe and the liquid flowing through. The main difference is because the experimental setup uses a drain pipe for filling, while the simulation assumes that the water flow is from the outlet of the drain pipe. The computational models do not simulate the entry of the liquid from the inlet of the drain pipe.

To remedy that problem, the flow rate was increased. A 12.6 cc/sec flow rate was set for the initial tests with the liquid test experimental setup. The desired flow rate was then set by adjusting the metering valve and collecting water in a beaker and measuring its weight. This procedure was repeated until a repeatable result was achieved. Then the stainless-steel flex hose was connected to the assembly, and the measurements were taken.

A-3.1.2 Overall Data

Four test runs were made with water. The level sensor data and volume data acquired during the experiment are shown in Figure A-12. The volume was calculated based on the reading of the digital scale.

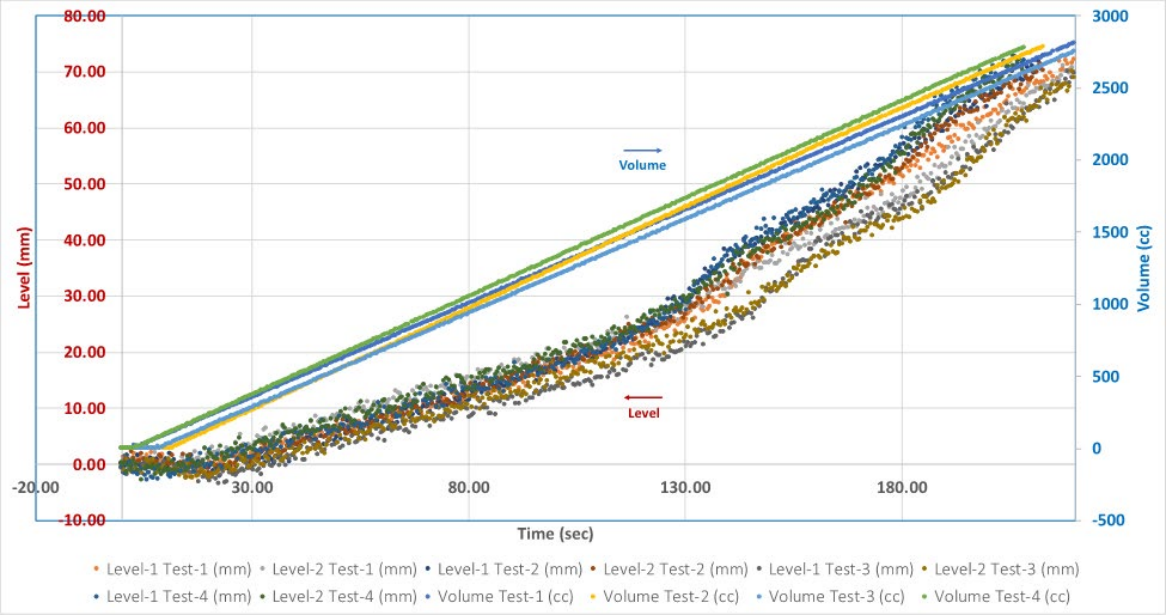

Figure A-12. Raw Experimental Data for Water Filling.

The level sensor data exhibited unexpected anomalies which are discussed in further detail below. The weight measurement was found to be highly reliable, although it also exhibited fluctuations about the measurement point during the filling process. A detailed measurement uncertainty quantification has not yet been conducted.

Uncertainties arise from the limitations of the experimental setup. One example is the onset of the filling process: the timer of the data acquisition (DAQ) system is started synchronously with the opening of the valve manually. However, there is currently no means in the experimental setup to consider the transport delay of the fluid in the flexible hose and the drain pipe. Therefore, these shortcomings inevitably create measurement uncertainties, and they are difficult to quantify. Attempts were made to alleviate these shortcomings through repeat experiments and by comparison of redundant and diverse sensor readings.

A-3.1.3 Volumetric Fill

Water volume was calculated based on the weight change. This section only discusses data from one of the test runs. The time-series data of the calculated water volume from Test #1 is shown in Figure A-13.

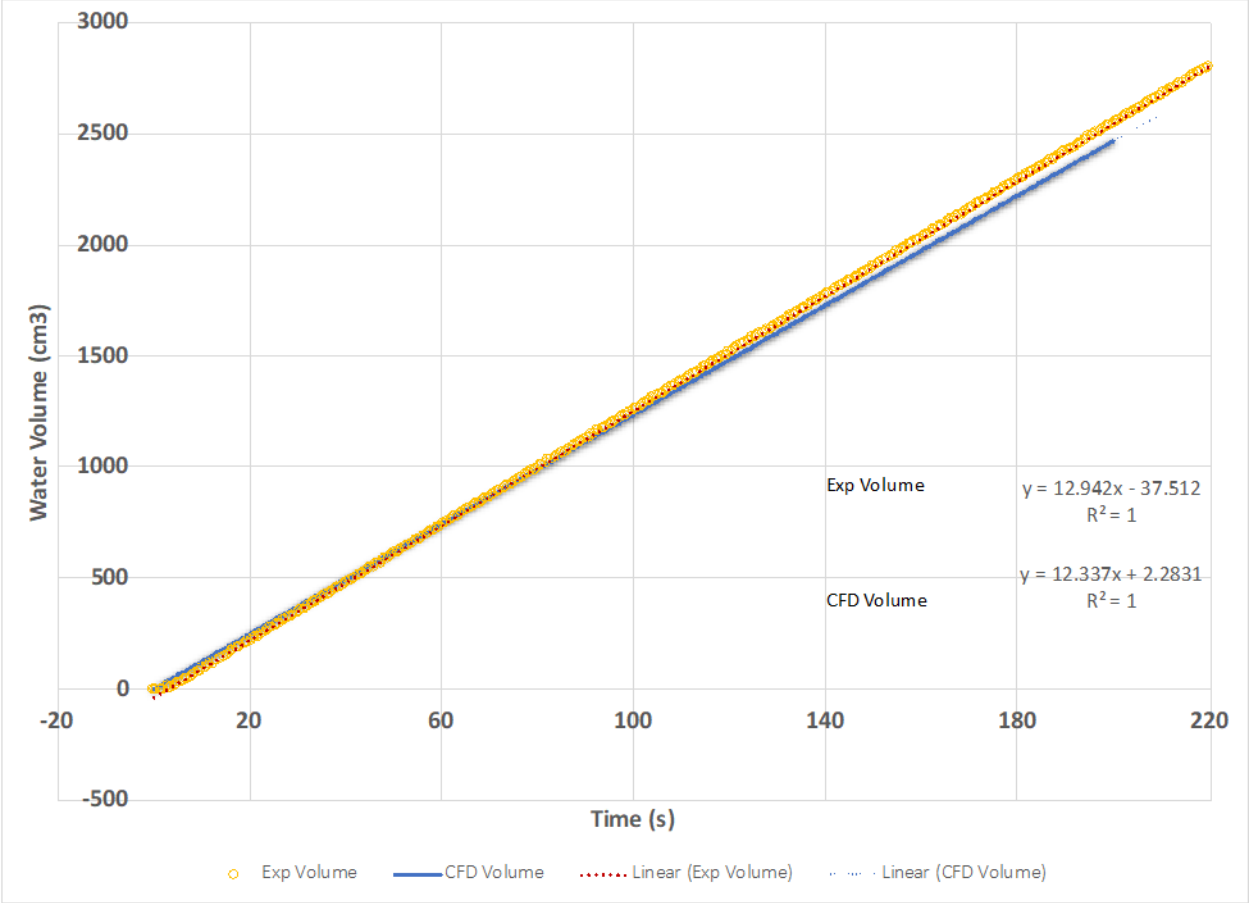

Figure A-13. Volumetric Fill Data as a Function of Time.

The linear regression to the experimental data yielded the following expression:

$$V = 12.942\, t - 37.512, \tag{18}$$

where t is time in sec, and V is the volume in cm^3. The slope of this equation yields the volumetric fill rate, which is q=12.942 cm^3/s.

The best way to observe the noise in the volume data is to look at the time differential of the time-series data as shown in Figure A-14. As the volumetric flow rate never changes during the fill process, this should ideally be a flat signal. However, as seen in the Figure A-14, the raw differential signal exhibits too much fluctuation. To reduce the noise level in the data, moving average filters of various orders have been tested. Ideally, this signal should be a flat line (i.e., a zero slope), and the constant value should be identical to the volumetric fill rate of q=12.942 cm^3/s.

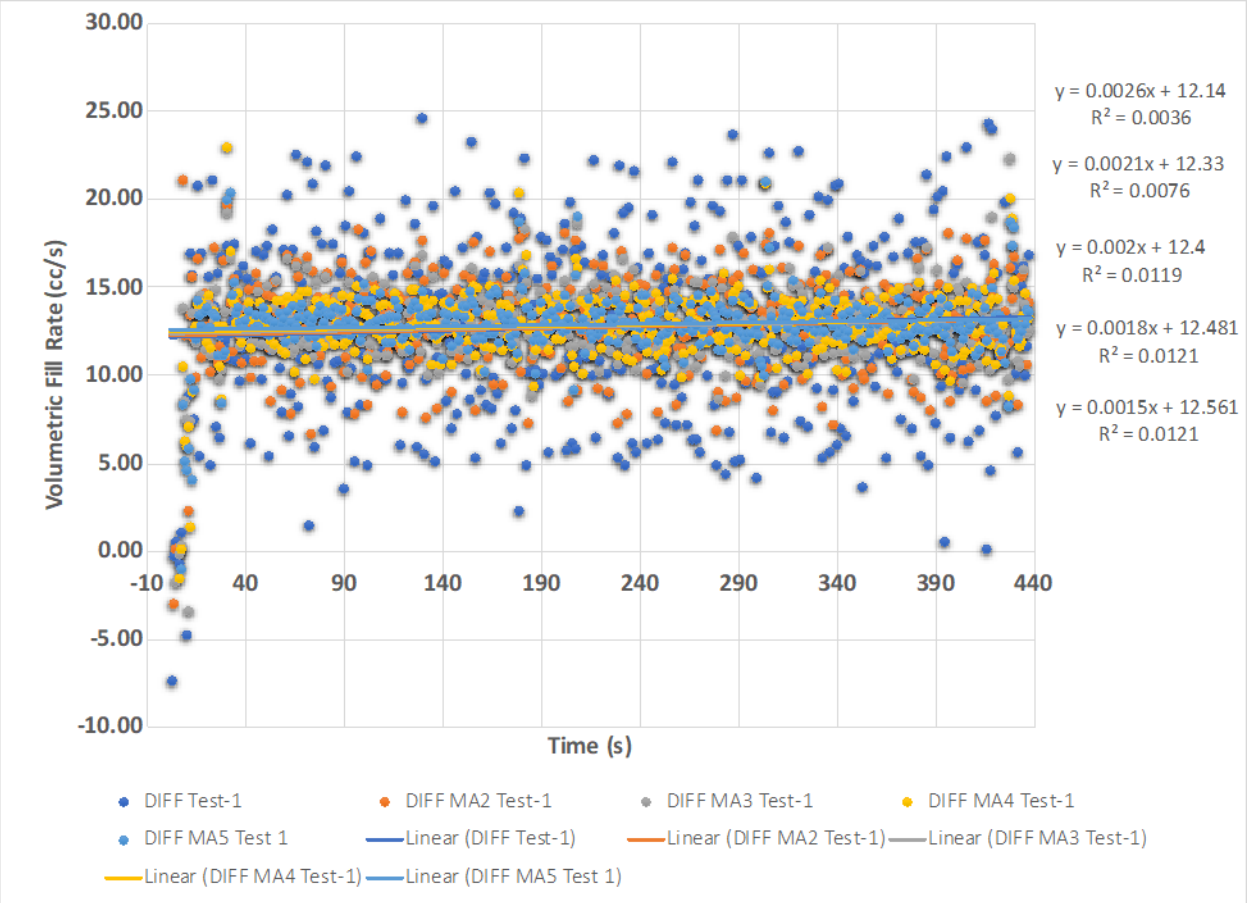

Figure A-14. Volumetric Fill Rate as a Function of Time.

The time differential of the raw signal yields a volumetric fill rate of 12.14 cm^3/s, which is significantly lower than the nominal fill rate. A moving average filter of the 5th order, on the other hand, yields the following expression:

$$q = 0.0015t + 12.561 \tag{19}$$

with a correlation coefficient of $R^2 = 0.0121$, which is still quite low, and which is an indication of highly uncorrelated noise content. No higher order moving-average filter was created, but this shortcoming of the scale was noted.

There may be a number of root causes to this observation:

1. The scale is placed on top of a low-mass table; most likely the table weighs less than the experimental setup. Therefore, it does not dampen the ground disturbances.
2. The height of the experimental setup potentially amplifies the impact of ground disturbances.

These observations and the experimental shortcomings will be addressed in the later phases of the project.

A-3.1.4 Level

As described earlier in the report, the experimental setup employs two level sensors. The raw data from Test #1 are shown in Figure A-15. The discrepancy between two sensors is notable.

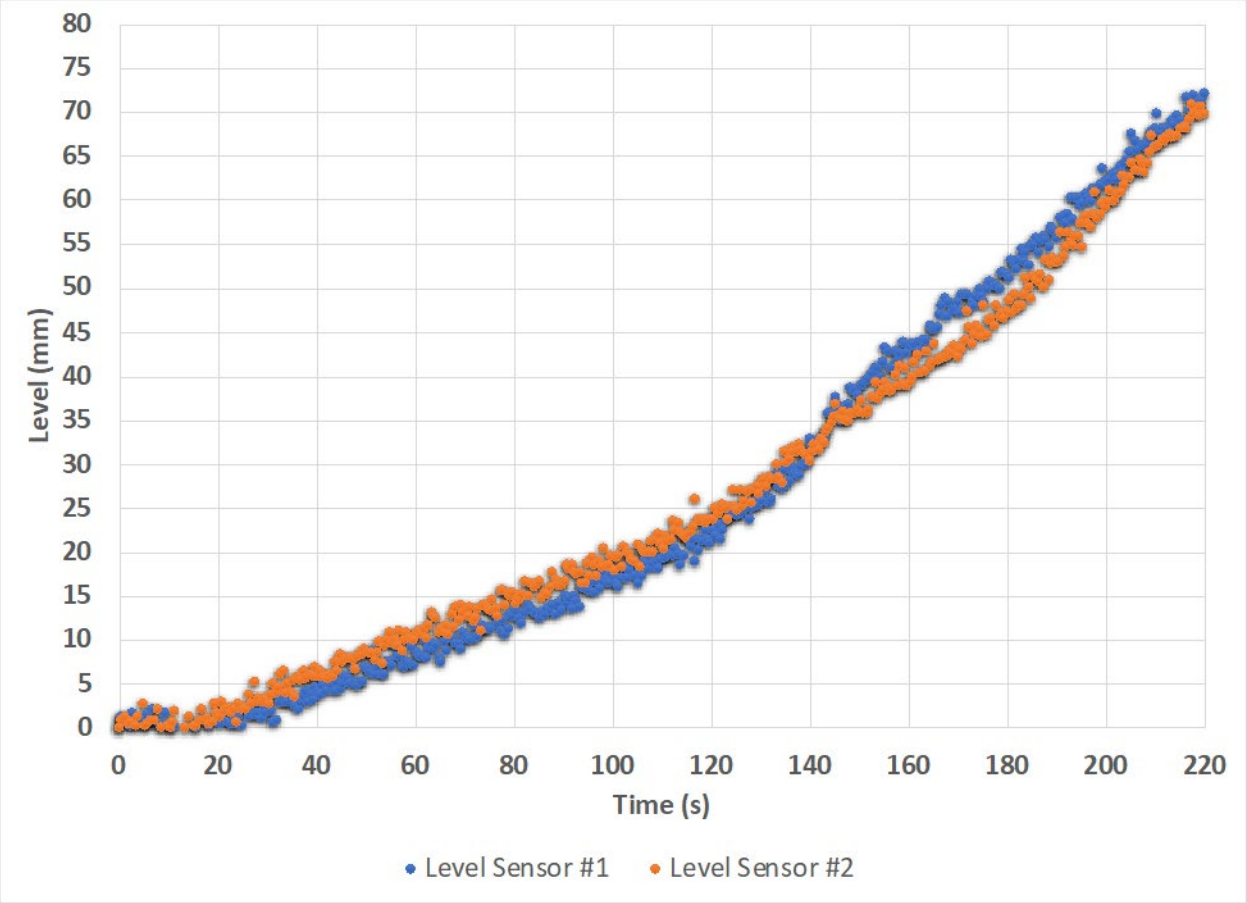

Figure A-15. Water-Level Data from the Two Redundant Level Sensors.

The time differential of the level sensor time-series data is shown in Figure A-16. Clearly, sensor #2 has significant noise content. As this observation was made, readings from this sensor were not considered reliable.

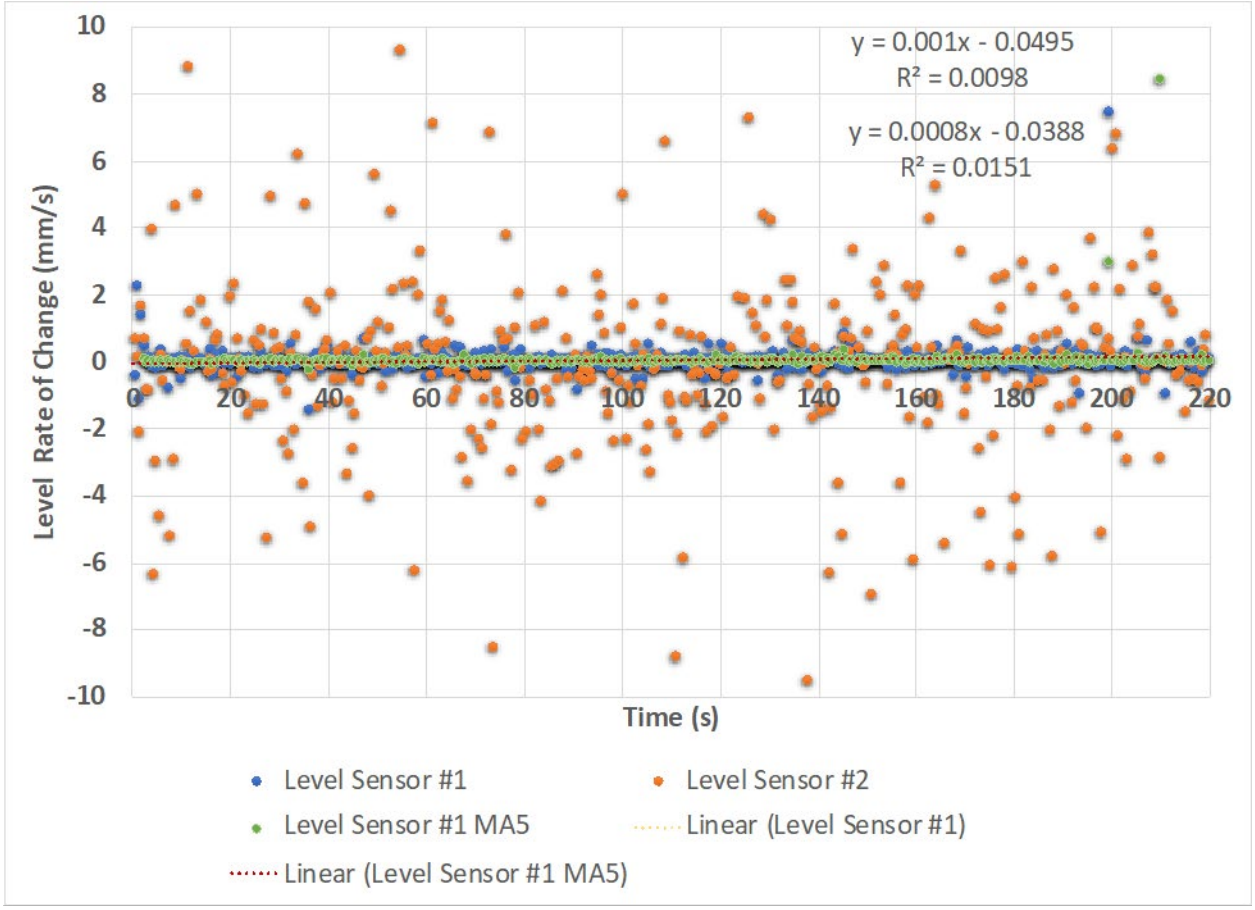

Figure A-16. Time Differential of the Raw Level Sensor Data.

A linear regression on level sensor #1 yields the following expression:

$$\dot{h} = 0.001\, t - 0.0495, \tag{20}$$

where $\dot{h}$ stands for rate of change in water level. Based on this expression, the fill rate is 0.0495 mm/s. The rate of the change in the level is a function of the geometric features of the experimental setup. Therefore, assigning a nominal rate would not be reasonable. However, the linear regression of the sensor data should have yielded the time average fill rate, i.e., as 70 mm was filled in 220 sec, the average nominal level fill rate should be

$$\langle \dot{h} \rangle = 0.32\ \frac{mm}{s}. \tag{21}$$

Even a fifth-order moving average filter was unable to improve the necessary signal quality.

Both sensors may have been affected by interference from the nearby metal walls. These observations were noted and are being investigated and addressed by the experiment team.

A-3.1.5 Comparison with CFD Data

The simulated and experimentally measured water levels are shown in Figure A-17. While the volume time-series data in Figure A-17 show a good agreement between the simulated and measured data, the level data between the two datasets are not consistent.

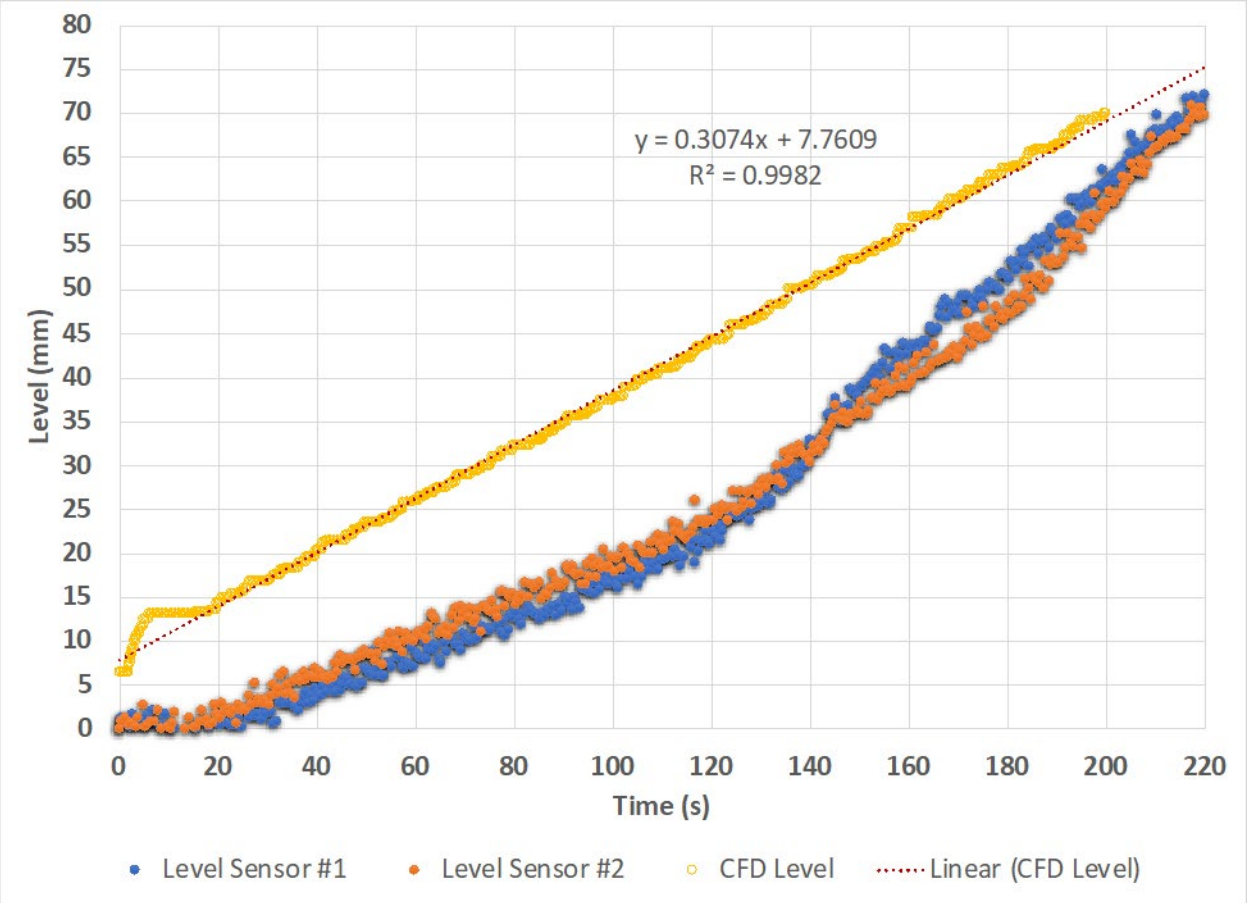

Figure A-17. Comparison of Measured and Simulated Water Levels as a Function of Time.

The level sensor stability is considered to be questionable: this issue is being investigated.

A-3.2 Water Experiment with Blockage

After completion of the initial testing with water, the mouse holes by the drain pipe were closed to represent a blockage scenario. Figure A-18. shows the blocked mouse holes by the drain pipe. Weight data are collected in real time through the data acquisition system, where the level rise was recorded by two separate cameras—one by the drain pipe, and the other placed 180° across from the drain pipe.

Figure A-18. View of the Blocked Mouse Holes by the Drain Pipe.

Figure A-19. shows a snapshot view of the filling recorded with a camera positioned across from the drain pipe. The elapsed time is recorded for every 1 mm rise inside the canister from the video recorded.

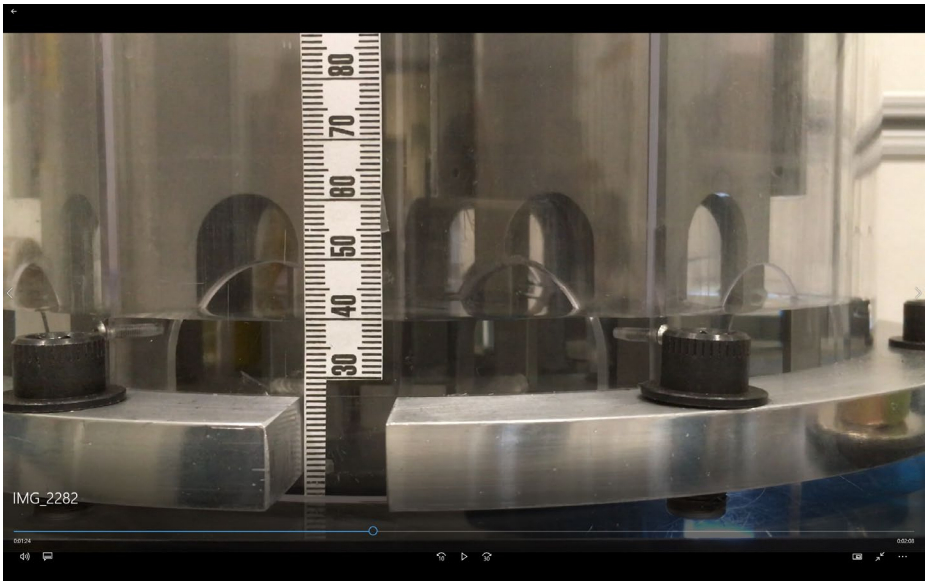

Figure A-19. Snapshot of the Filling Camera Recording Positioned 180° across from the Drain Pipe.

The raw data collected from both the open channel filling and the blocked channel filling are shown in Figure A-20. through Figure A-22. Figure A-20 shows the first 110 seconds of the filling process. The measurements indicate that it takes longer to fill in the open channel experiment than in the blocked channel experiment.

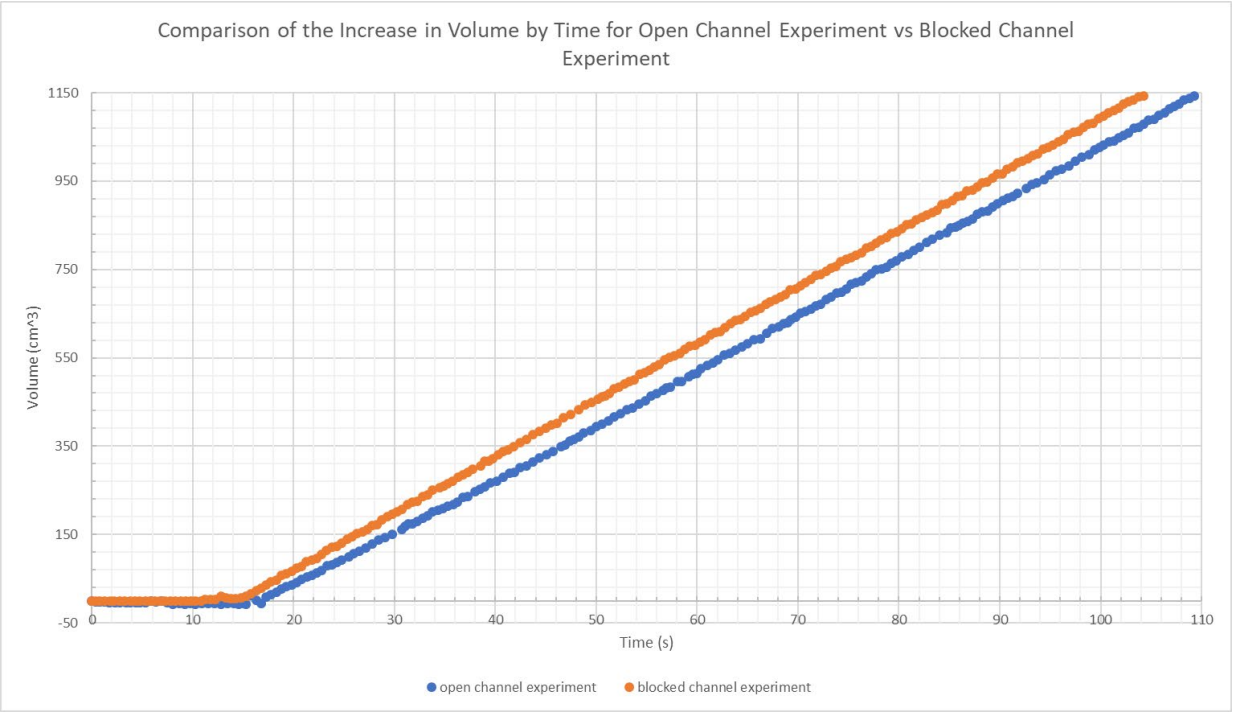

Figure A-20. Comparison of the Water Filling Time.

The raw level progression data also show that the level increase takes slightly longer in the open channel experiment than in the blocked channel experiment since there is slightly more volume to be filled in the open channel experiment. A practical use of this data would be understanding if there is a blockage in the real filling application out in the field. Currently, the data collected from those preliminary measurements are under evaluation. Further findings will be reported in the future.

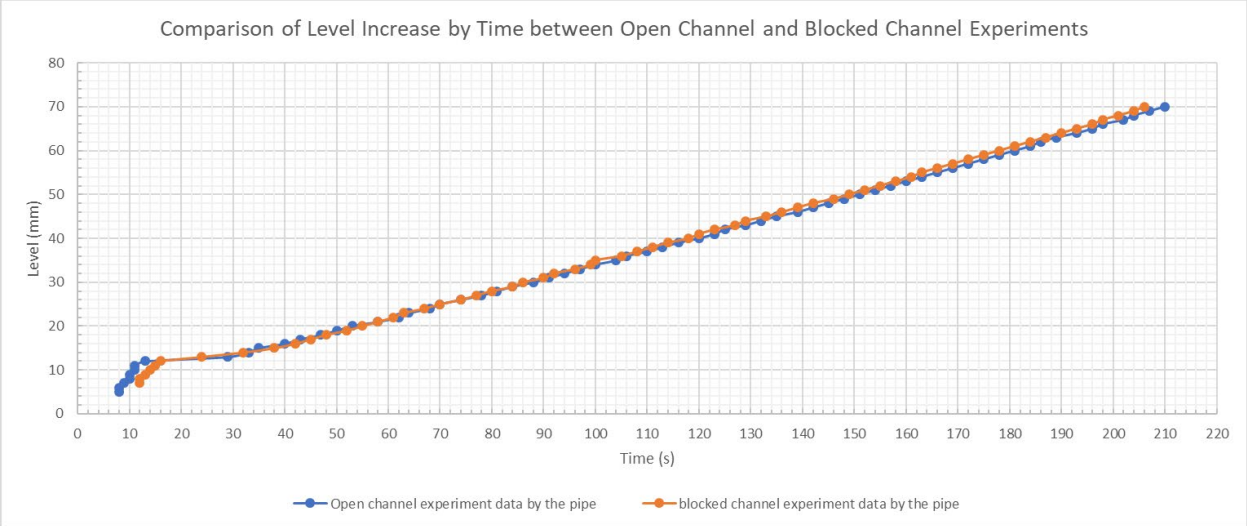

Figure A-21. Comparison of the Level Increase as a Function of Time Monitored by the Pipe.

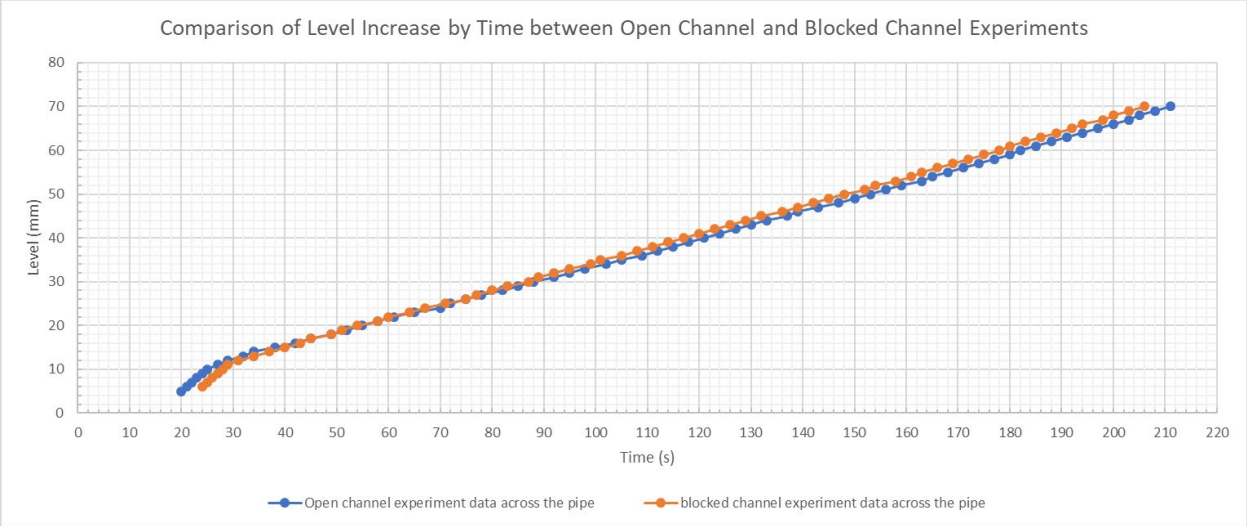

Figure A-22. Comparison of the Level Increase as a Function of Time Monitored across the Pipe.

A-3.3 Glycerin Experiment

Using 5 gallons of glycerin, the prior experiment described above was repeated using the highly viscous fluid. The density of glycerin is 1.26 g/cc, and the dynamic viscosity is 1.412 Pa-s at around room temperatures. The experimental set up was modified for injecting the glycerin at a constant flow rate. The glycerin was held inside a bladder reservoir which was contained inside a large container. Plate weights were applied to the bladder (22.5 kg) to apply a head pressure to the glycerin bladder. The spout on the bladder was connected to the outlet of the reservoir with a valve to eliminate back flow and to allow for adjustment of the desired flow rate of glycerin out of the container. The glycerin test system is shown in Figure A-23. For the initial testing, two cameras at opposite angles were used to record and measure the glycerin level as it fills. As in the water experiment, the mass/volumetric flow of glycerin into the DPC apparatus was measured in real time using Labview software to record the increasing weight of the apparatus as it filled with glycerin.

The guide pulse sensor will be used in future testing after the stability issue is addressed by modifying the obstacles in the proximity of the detection zone.

Figure A-23. Glycerin Test System Set Up.

Figure A-24 and Figure A-25 display the data collected from the initial test for filling the liquid test system with glycerin. Figure A-24 shows the filling volume increase by time. The flow rate was calibrated to 11.77 cc/sec by adjusting the metering valve at the spout of the reservoir. After the weight data was collected using the scale, the volume was calculated at each time interval. The linear trendline was fit, and the flow rate was found to be 5.18 cc/sec. Since the glycerin is much more viscous than water, it is clear that the friction inside the flex hose and the drain pipe reduced the flow rate during the filling. Data collection started before the main valve was opened to start filling process. Therefore, the initial volume values do not start from zero, so those values can be neglected.

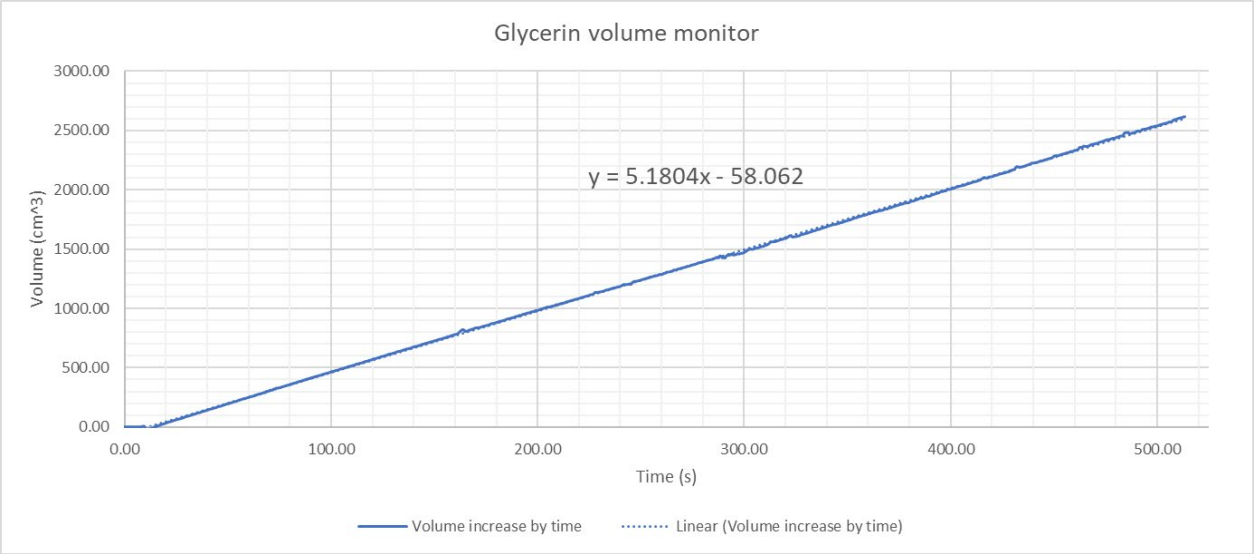

Figure A-24. Glycerin Filling Volume as a Function of Time.

Figure A-25 shows the level increase during filling as taken by two cameras. One camera was placed to monitor the filling by the pipe, and another camera was placed to monitor the level at 180° across from the pipe. The time difference between the rise of the level at the two locations is clearly different as expected due to the glycerin's higher viscosity.

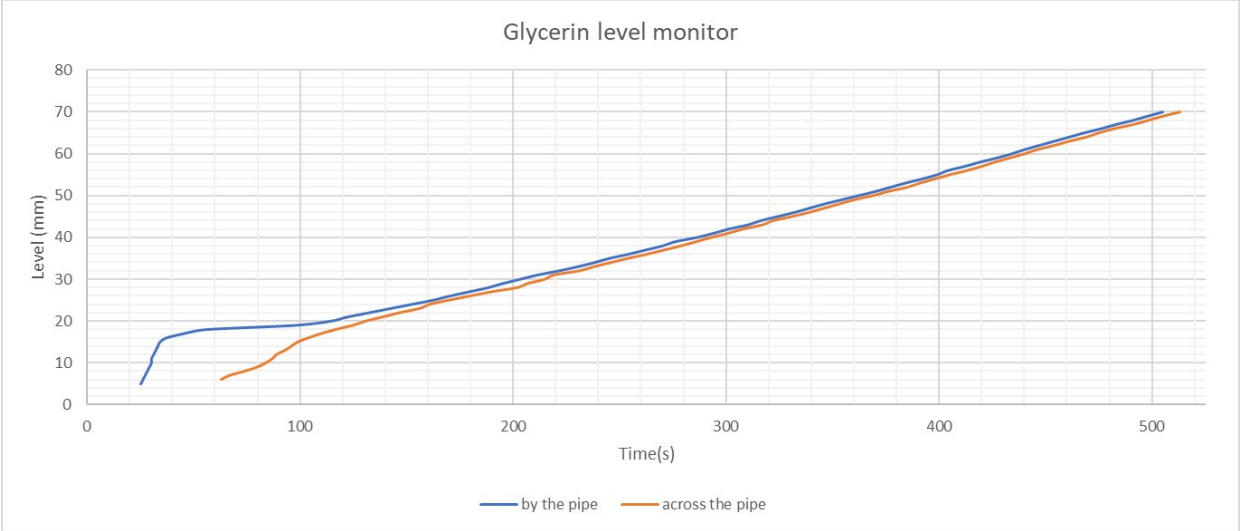

Figure A-25. Glycerin Filling Level Increase by Time.

A-3.4 Paraffin Experiment (In Progress)

The experimental setup of the paraffin experiment is similar in structure to the previously completed water and glycerin experiments. Figure A-26 shows the set up. However, this apparatus must incorporate a source of heat to keep the paraffin in a liquid state during the entirety of the filling process. Solid paraffin is first heated inside a large stainless-steel reservoir beyond the melting point.

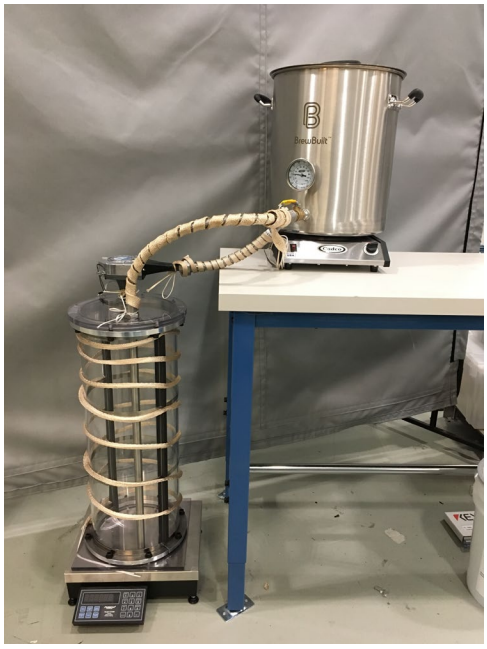

Figure A-26. Paraffin Experiment Set Up.

While this paraffin heating process is taking place, the DPC canister will also be heated using heat tape and a recirculation blower. The heat tape will warm the braided tubing as shown in Figure A-27 below, which will be recalculated through the three-way valve and directed back into the DPC canister. This constant heating and air circulation will heat the canister and its internal components in excess of the melting point of paraffin to prevent premature solidification of the paraffin once the filling process begins.

Once the paraffin is in its liquid state and the canister is preheated, the three-way valve will be adjusted to turn off the recirculation of air and to allow the inflow of liquid paraffin through the drain tube and into the canister. The paraffin will be allowed to completely fill the canister before the heat tape is turned off and the paraffin allowed to cool and solidify.

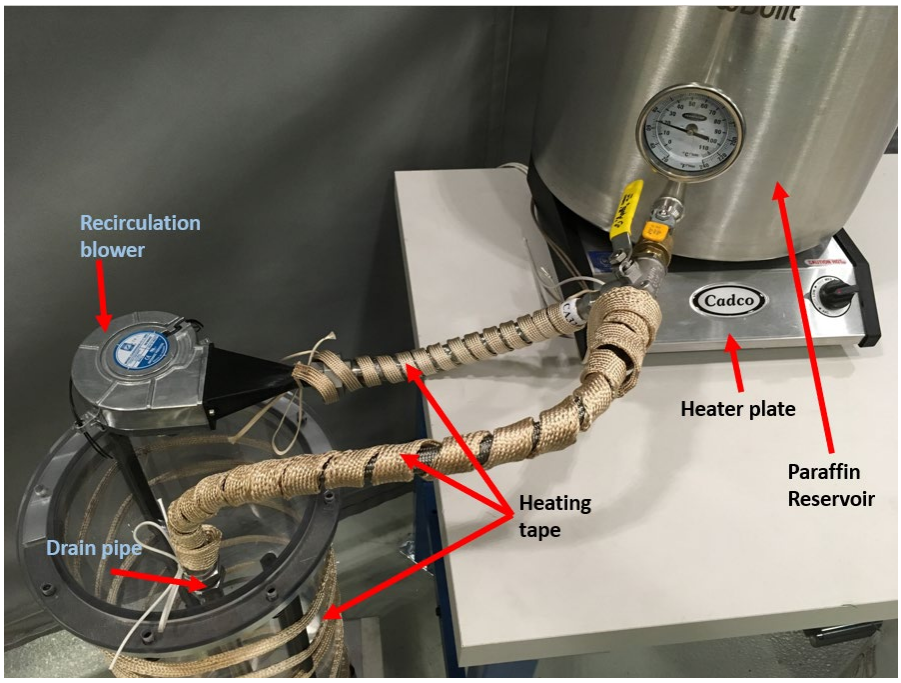

Figure A-27. Paraffin Experiment Parts.

Once the paraffin is completely solidified, the outer canister will be disassembled, and then the inner components, including the modular spacer grid shown in Figure A-28, can be disassembled and checked for filling efficiency and any voids that may be present. The grids are shown assembled using 3D printed plastic top and bottom plates. Metal plates that will essentially be used for assembly are still in fabrication.

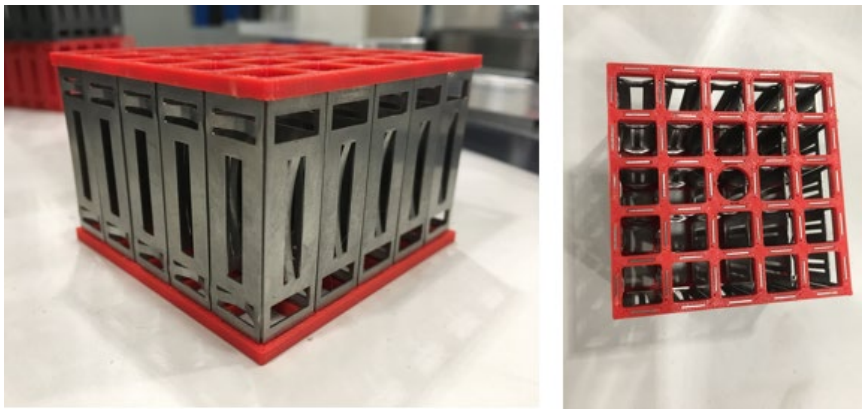

Figure A-28. Modular Spacer Grids.

A-4. Conclusions

Experiments with water and glycerin are ongoing. Necessary test system modifications have been identified and in progress. Analysis of the data in hand is ongoing. The planned future experiments are grouped into two categories: (1) the experiments that deal mainly with the filling process (flow)—water, glycerin, honey, mineral oil, etc., and (2) experiments that provide information about the thermal effects— paraffin, liquid metal, etc. The flow characteristics are being explored through modeling and experiments, while the thermal effects are yet to be characterized by modeling. The thermal experiments will be performed to address the solidification process, void spaces during filling and cooling, cracking

due to nonuniform cooling, surface tension, etc. After the paraffin experiments have identified potential areas where there could be void spaces in the filling process, the same experiments will be performed with liquid metal. A nontoxic, low melting point metal such as tin, which has a melting point of 231.9°C, will be used to understand the solidification process using the actual spacer grid but with a reduced length of the fuel rods. Once the test sample is externally heated using heating tape and recirculating hot gas to establish a constant temperature, melted tin will be poured in. The temperature of the blanket will be reduced in a slow and controlled manner to reduce the possibility of cracking from differential temperature over the region. Once the experiment is complete, the sample will be analyzed in detail by sectioning it along various axes.

A-5. References

1. Holtec International, *Final Safety Analyses Report for the HI-STORM 100 Cask System*, (2010).
2. N. A. Weichselbaum et al., *Surrogate Spacer Grid Design for Fluid-Structure Interactions Studies in Fuel Bundles*, The George Washington University, Washington, DC (2015).
3. Keyence Corporation Sensing Guide Pulse Level Sensor https://www.keyence.com/products/process/level/fl/index.jsp.